Serotonin suppresses slow oscillations by activating somatostatin interneurons via the 5-HT$_{2A}$ receptor

Roberto De Filippo[1], **Benjamin R. Rost**[2], **Alexander Stumpf**[1], **Claire Cooper**[1], **John J. Tukker**[1,2], **Christoph Harms**[3-5], **Prateep Beed**[1], **Dietmar Schmitz**[1,2,5*]

[1] Charité – Universitätsmedizin Berlin, Neuroscience Research Center, 10117 Berlin, Germany
[2] German Centre for Neurodegenerative Diseases (DZNE), 10117 Berlin, German
[3] Charité – Universitätsmedizin Berlin and Berlin Institute of Health, Department of Experimental Neurology, 10117 Berlin, Germany.
[4] Charité – Universitätsmedizin Berlin, Center for Stroke Research Berlin, 10117 Berlin, Germany
[5] Charité – Universitätsmedizin Berlin, Einstein Center for Neurosciences Berlin, 10117 Berlin, Germany

* Correspondence to: dietmar.schmitz@charite.de

Keywords: serotonin, 5-HT$_{2A}$, somatostatin interneurons, slow oscillations, MDMA, entorhinal cortex

Abstract

Serotonin (5-HT) affects multiple physiological processes in the brain and is involved in a number of psychiatric disorders. 5-HT axons reach all cortical areas; however, the precise mechanism by which 5-HT modulates cortical network activity is not yet fully understood. We investigated the effects of 5-HT on slow oscillations (SO), a synchronized cortical network activity universally present across species. SO are observed during slow-wave sleep and anesthesia and are considered the default cortical activity pattern. Combining opto- and pharmacogenetic manipulations with electrophysiological recordings, we discovered that 5-HT inhibits SO within the entorhinal cortex (EC) by activating somatostatin-expressing (Som) interneurons via the 5-HT$_{2A}$ receptor (5-HT$_{2A}$R). This receptor is involved in the etiology of different psychiatric disorders and mediates the psychological effects of many psychoactive serotonergic drugs, suggesting that 5-HT targeting of Som interneurons may play an important role in these processes.

Introduction

5-HT is one of the most important neuromodulators in the central nervous system. Projections originating from the Raphe nuclei, the brain-stem structure that comprises the majority of 5-HT releasing neurons in the brain, reach all cortical and sub-cortical area (Descarries et al., 2010). Consequentially, it is not surprising that 5-HT is involved in the regulation of a myriad of physiological functions (e.g. circadian rhythm, mood, memory formation, reward encoding, sexual behavior) and psychiatric disorders including depression, autism, schizophrenia, and anxiety disorders (Monti, 2011, Underwood et al., 2018, Hayes and Greenshaw, 2011, Teixeira et al., 2018, Uphouse and Guptarak, 2010, Nakai et al., 2017).

5-HT levels in the brain are closely linked to the sleep-wake cycle. Activity of serotonergic raphe neurons is increased during wakefulness, decreased during slow-wave sleep and virtually silent during REM sleep (McGinty and Harper, 1976, Oikonomou et al., 2019). Cortical activity is also influenced by the behavioral state of the animal: slow-wave sleep (SWS) is generally associated to "synchronized" patterns of activity, characterized by low-frequency global fluctuations, whereas active wakefulness and REM sleep features "desynchronized" network activity in which low-frequency fluctuations are absent. The shifting of cortical networks between different patterns of activity is controlled, at least in part, by neuromodulators (Lee and Dan, 2012). For instance, Acetylcholine (Ach) can profoundly alter cortical network activity by inducing desynchronization via activation of Som interneurons (Chen et al., 2015). However, it is not solely responsible for cortical desynchronization as lesions of cholinergic neurons are not sufficient to abolish desynchronization (Kaur et al., 2008). On the other hand, blocking Ach and 5-HT transmission at the same time causes a complete suppression of cortical desynchronization, even during active behavior, thus suggesting that 5-HT plays an important role in desynchronization (Vanderwolf and Baker, 1986). In agreement with this line of thought, electrical and optogenetic stimulation of the Raphe nuclei reduce low frequency (1-10 Hz) power in the cortex thus promoting desynchronization (Puig et al., 2010, Grandjean et al., 2019). Moreover, optogenetic stimulation of serotonergic neurons at a physiological frequency (25 Hz) is sufficient to wake up mice from SWS (Oikonomou et al., 2019). These data suggest a causal relationship between 5-HT levels and cortical activity (Lee and Dan, 2012, Harris and Thiele, 2011). The exact mechanism by which 5-HT modulates network activity in the cortex is, however, still not fully understood.

Here, we used electrophysiological techniques together with pharmacology, optogenetics and pharmacogenetics to investigate the effect of 5-HT on SO, a network oscillation

characterized by synchronized transitions (< 1 Hz) between periods of high activity (up-state) and relative quiescence (down-state) (Steriade et al., 1993, Neske, 2015). SO are a global phenomenon observed throughout the cerebral cortex and are considered to be the default emergent activity of cortical networks during slow wave-sleep and anesthesia (Neske, 2015, Sanchez-Vives et al., 2017). Our results show that 5-HT release *in vivo* is sufficient to suppress SO and, concurrently, activate a small group of neurons characterized by an intermediate waveform shape. Using cortical brain slices, we were able to characterize the 5-HT activated neurons as Som-expressing interneurons and show that they are necessary mediators of the effect of 5-HT on SO *in vitro*. While previous studies have shown that parvalbumin (PV) interneurons are excited by 5-HT (Puig et al., 2010, Athilingam et al., 2017), our results identify cortical Som interneurons as novel targets of the 5-HT neuromodulatory system.

Results

5-HT inhibits SO *in vivo*

We investigated the effect of 5-HT on network activity in anesthetized mice using multisite silicon microelectrodes placed in the entorhinal cortex (EC), a region located in the medial temporal lobe interconnected to a variety of cortical and subcortical areas (Figure 1A-B, Figure 1–figure supplement 1) including the Raphe nuclei (Figure 1C) (van Strien et al., 2009, Muzerelle et al., 2016). Under urethane anesthesia, EC, like the rest of the cortex, displays SO (Figure 1–figure supplement 2). As expected, we found that up-states were present synchronously in the local field potential (LFP) of all the recording channels (Figure 1–figure supplement 3) and every up-state coincided with large increases in population spiking activity (Figure 1D). 5-HT does not cross the blood brain barrier (Hardebo and Owman, 1980), therefore, to understand the effect of 5-HT on SO we used (±)3,4-methylenedioxymethamphetamine (MDMA), a potent presynaptic 5-HT releaser and popular recreational drug (Green et al., 2003). Intraperitoneal injections of MDMA (1.25 mg/kg) caused a strong suppression of up-state incidence (Figure 1G-J), a decrease in power of delta frequencies (Figure 1H), and a reduction of population spiking activity (Figure 1I-K). MDMA also causes, although to a lesser extent, the release of dopamine and noradrenaline (Green et al., 2003). To test whether the effect of MDMA was mediated specifically by 5-HT we repeated the experiment using fenfluramine (Fen) (5 mg/kg), a more selective 5-HT releaser (Rothman and Baumann, 2002). Intraperitoneal injection of Fen had a comparably strong suppressive effect on both the occurrence of up-states and

population spiking activity (Figure 1J-K). This shows that 5-HT released from raphe neurons is capable of modulating ongoing oscillatory activity and suppress low-frequency fluctuations.

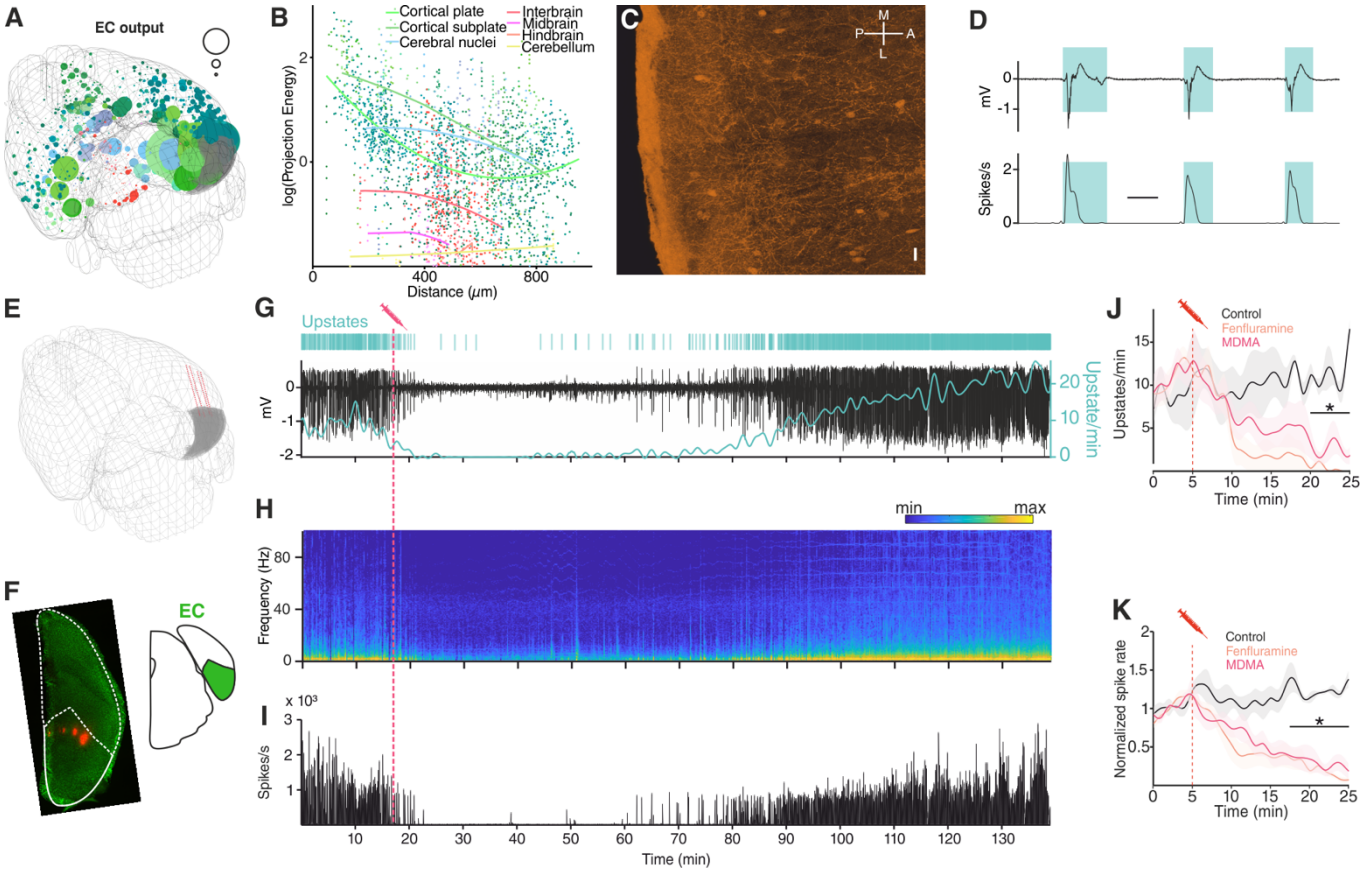

Figure 1| MDMA inhibits SO *in vivo*. (A) Map of EC output connectivity registered to the Allen mouse common coordinate framework. Circle size represents projection energy (see "Supplementary Materials and Methods"). Circle color encodes area location according to the Allen institute standard: green = cerebral cortex, blue= cerebral nuclei, pink = midbrain, red = interbrain/hindbrain and yellow = cerebellum. (B) Scatter plot showing relationship between projection distance and projection energy. (C) Immunostaining of an ePet-YFP mouse showing serotonergic fibers in medial entorhinal cortex, horizontal slice (M = medial, L = lateral, P= posterior, A = anterior). Scale bar: 20 μm. (D) LFP (top) and instantaneous population activity (bottom) of a representative *in vivo* recording during SO (spikes/s units in thousands), cyan rectangles represent detected up-states. (E) 3D visualization of the microelectrode location of the recording shown in g. EC represented in grey. (F) Left: microelectrode tracks (red) of the recording shown in (G). Right: EC position represented in green. (G) Top: Cyan lines represent detected up-states. Bottom: LFP (black) and average up-state incidence per minute (cyan). Pink dotted line represents MDMA application time. (H) Fourier transformation and (I) instantaneous population activity for the recording shown in G (spikes/s units in thousands). (J) Mean up-state incidence after saline (control), Fen or MDMA application (control: n = 5, Fen: n = 6, MDMA: n = 7; $p < 10^{-4}$, unpaired t test with Holm-Sidak correction). (K) Mean normalized spike rate after saline (control), Fen or MDMA application (control: n = 5, Fen: n = 6, MDMA: n = 7; $p < 10^{-4}$, unpaired t test with Holm-Sidak correction).

5-HT activates a subgroup of cortical neurons

Besides the LFP signal, we recorded the activity of 355 single units within the EC. Because of the very similar effects of MDMA and Fen on spike rates (Figure 1K), we pooled all units recorded in both types of experiments. We found that drug injections differentially affected

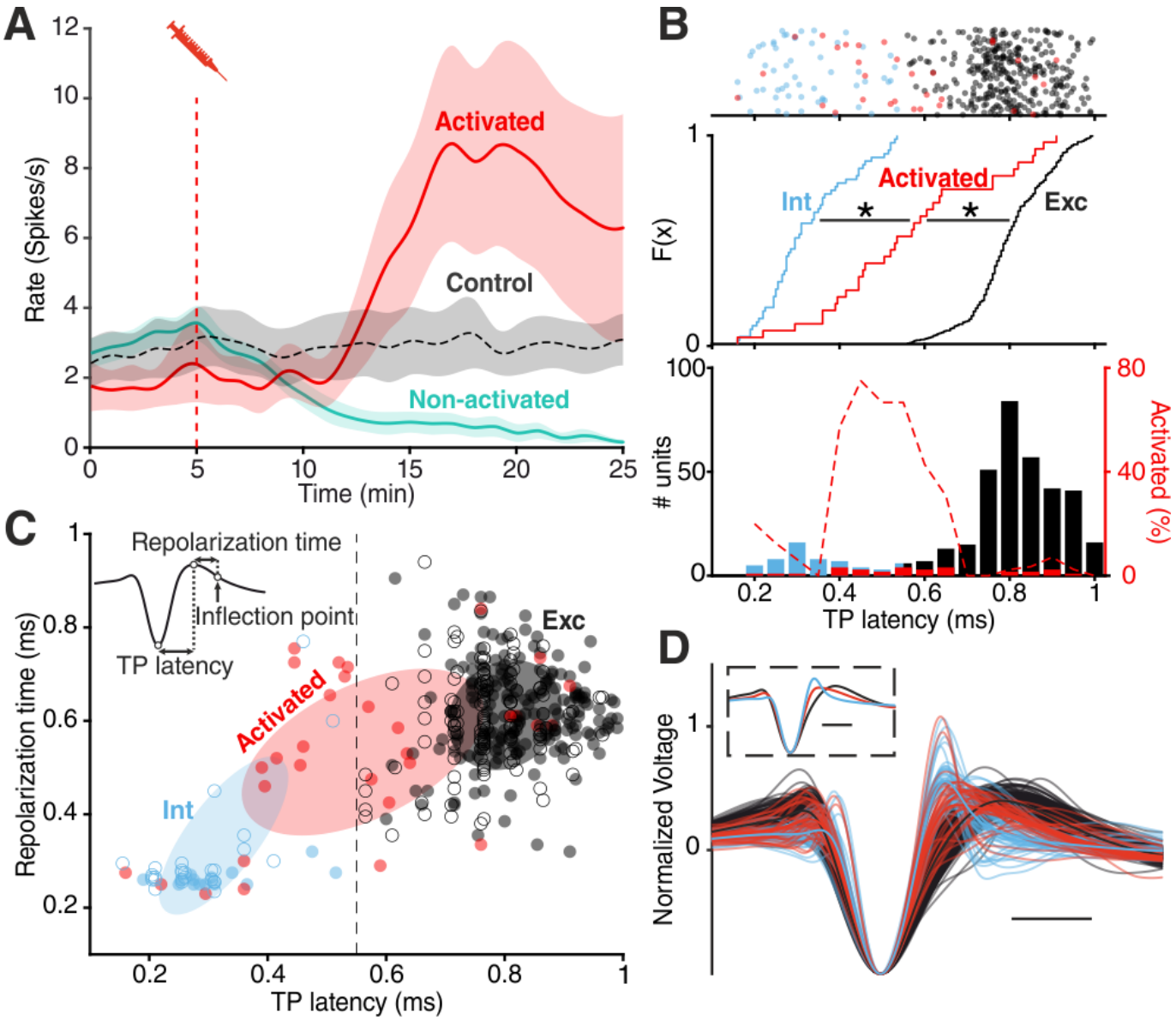

Figure 2| Divergent unit responses to MDMA/Fen application. (A) Spike rate of the activated units versus all the other units during MDMA/Fen application (activated: n = 31, Non-activated: n = 324). (B) Top: TP latencies color-coded by group. Middle: cumulative distribution of TP latencies (Kolmogorov-Smirnov test, $p_{Activated\ vs\ Int} < 10^{-4}$, $p_{Activated\ vs\ Exc} < 10^{-4}$). Bottom: bar plot representing probability distribution of TP latencies, on the right y axis dashed line representing the percentage of 'activated' units per TP latency bin. (C) Distribution of units according to trough-to-peak (TP) latencies and repolarization time, units were classified as putative interneurons (Int, blue) and putative excitatory (Exc, dark gray) according to a threshold at 0.55 ms; activated units (red) could belong to either group but were mostly intermediate as shown by the covariance (2 STD) of each group (Ellipses). Units recorded during control experiments are represented by empty circles. (D) Waveforms of recorded units (n= 355). Units were divided into "putative excitatory" (black) and "putative inhibitory" (blue) neurons according to TP latencies. Units activated either by MDMA or Fen application are represented in red. Inset shows the average waveform for each group. Scale bars: 0.5 ms.

spiking rates (Figure 2A) of recorded units: while spiking decreased in the majority of units ('non-activated'), a small group of units ('activated') responded in the opposite fashion (n=31/355, 8,7%).

Trough-to-peak (TP) latency of the spike waveform has been consistently used as a metric to classify units and, in accordance with previous studies (Senzai et al., 2019, Roux et al., 2014), we found a clear bimodal distribution of TP latencies distinguishing putative excitatory (Exc) and fast-spiking inhibitory (Int) groups. Analysis of cross-correlograms to infer monosynaptic connections confirmed the inhibitory nature of a subset of putative FS units (Figure 2–figure supplement 1) (Barthó et al., 2004). The cumulative distribution of TP latencies of 'activated' units was significantly different to both Exc and Int groups (Figure 2B). Specifically, the average TP latency of 'activated' units was situated in between the Int and Exc groups (Figure 2B-D, Figure 2–figure supplement 2), possibly suggesting a non-fast spiking interneuron identity (Trainito et al., 2019, Kvitsiani et al., 2013).

5-HT suppresses SO and activates Som interneurons *via* 5-HT$_{2A}$R

To understand the mechanism underlying the suppression of SO by 5-HT we combined electrophysiology and pharmacology *in vitro*. First, we recorded simultaneously from up to four neurons in the superficial layers of the EC (Figure 3A). Brain slices were perfused with an extracellular solution containing Mg^{2+} and Ca^{2+} in concentrations similar to physiological conditions. With this method we could reliably detect SO reminiscent of the *in vivo* network activity (Tahvildari et al., 2012). Release of 5-HT *in vitro*, induced by Fen application, caused a suppression of SO similar to what we observed *in vivo* (Figure 3–figure supplement 1). Likewise, application of low concentrations of 5-HT (5 µM) caused a suppression of SO (Figure 3B, C). This effect was highly consistent across different slices and was readily reversible (Figure 3D). Similarly to spontaneous up-states, electrically evoked up-states (Neske et al., 2015) were also suppressed by 5-HT (Figure 3–figure supplement 2). Increasing the stimulation intensity did not rescue up-state generation, indicating that lack of excitation alone cannot explain the suppressive effect of 5-HT on SO.

Suppression of activity can have either an intrinsic or synaptic origin (Turrigiano, 2011). A substantial subset of EC excitatory neurons is known to express 5-HT$_{1A}$ receptor (5-HT$_{1A}$R) and hyperpolarize upon 5-HT application via activation of G protein-coupled inwardly-rectifying potassium (GIRK) channels (Figure 3–figure supplement 3E) (Schmitz et al., 1998, Chalmers and Watson, 1991). SO suppression, however, was not influenced by blocking 5-HT$_{1A}$R (Figure 3–figure supplement 3A, F). In contrast, blocking 5-HT$_{2A}$R with the selective antagonist ketanserin (Preller et al., 2018) strongly reduced the suppression power of 5-HT on SO from 95 ± 4% to 57 ± 10.1% (Figure 3–figure supplement 3B, F). The remaining suppression can be possibly explained by the activation of 5-HT$_{1A}$R on excitatory cells, this is reflected by the

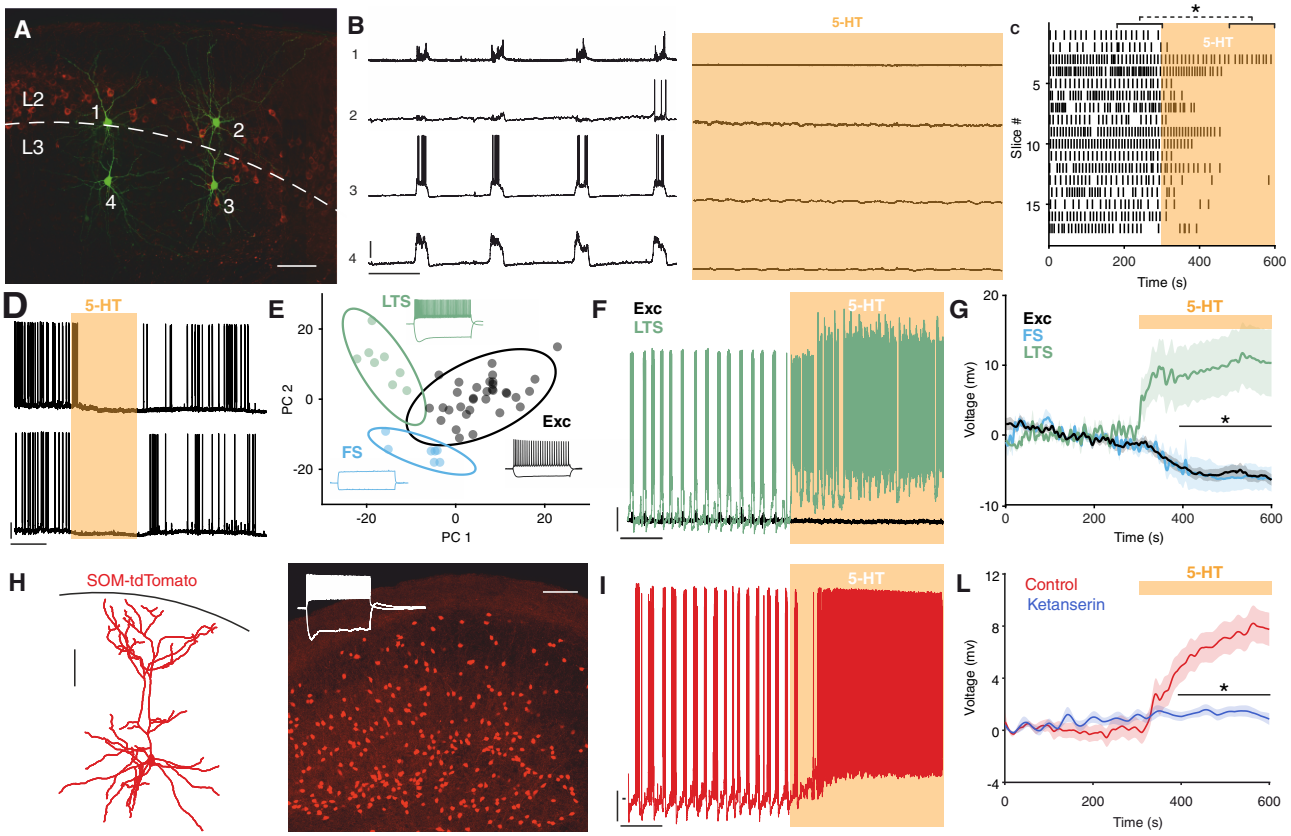

Figure 3| 5-HT suppresses SO and activates Som interneurons. (A) Biocytin staining of four simultaneously recorded cells shown in (B) WFS1 expression (in red) delimits L2/3 border. (B) Intracellular recordings showing synchronous up-state events in 4 simultaneously recorded cells before (left) and after (right) 5-HT application. Scale bars: 1: 7.5 mV, 2: 25 mV, 3: 25 mV, 4: 10 mV; 10 s. (C) Up-state raster plot before and after 5-HT application, orange box represents 5-HT application (n = 17, $p < 10^{-4}$, Wilcoxon signed rank test). (D) Representative recording showing the temporary inhibitory effect of 5-HT on SO in two simultaneously recorded cells. Scale bars: 5 min, 20 mV. (E) PCA projection plot of all the cells recorded (n = 48). Cells are color coded according to group identity: Exc (black), FS (light blue) or LTS (green). Typical voltage responses to current injection (-150 and +250 pA) are plotted for each group. (F) Representative recording of an excitatory (black) and a low-threshold (green) neuron simultaneously recorded during 5-HT application. Scale bars: 10 mV, 30 s. (G) Average change of RP before and after 5-HT application, across excitatory, fast-spiking and low-threshold neurons (Exc: n = 34, FS: n = 6; LTS: n = 9; $p < 10^{-4}$, unpaired t test with Holm-Sidak correction). (H) Left: Reconstruction of a recorded Som interneuron. Scale bar: 100 µm. Right: tdTomato expression in EC in a slice from a Som-tdTomato mouse. Inset shows a representative Som interneuron response to current injection (-150 and +250 pA). Scale bar: 100 µm. (I) Representative recording of a Som interneuron during 5-HT application. Scale bars: 10 mV, 30 s. (L) Average RP of Som interneurons during 5-HT (red) and ketanserin +5-HT (blue) application, orange bar represents 5-HT.

reduced spiking activity of putative excitatory cells (Figure 3–figure supplement 3D). Selective activation of 5-HT_2R by α-methyl-5-HT could also replicate SO suppression (Figure 3–figure supplement 3C, F). Together, these results point to the importance of 5-HT_{2A}R in the suppression of SO.

177 5-HT_{2A}R activation causes an increase in intracellular calcium and consequent depolarization
178 of the resting potential (RP) (Nichols and Nichols, 2008). Accordingly, after 5-HT application, we
179 found that a small group of neurons was depolarized (n= 6/48, 12,5%) (Figure 3–figure
180 supplement 4). Using a soft clustering approach with six electrophysiological parameters (see
181 "Materials and Methods") we divided the recorded cells in 3 groups: Excitatory (Exc), fast-
182 spiking (FS) and low-threshold spiking (LTS) (Figure 3E, Figure 3–figure supplement 5).
183 Strikingly, the cells excited by 5-HT belonged exclusively to the LTS group (Figure 3G, Figure
184 3–figure supplement 4).
185 A substantial part of LTS neurons expresses Som (Tremblay et al., 2016, Gibson et al., 1999),
186 therefore we performed targeted patch-clamp recordings using a mouse line expressing
187 tdTomato specifically in Som-expressing interneurons (Figure 3H). Som interneurons
188 depolarized upon 5-HT application (n=19, ΔRP: 7.5 ± 1.23 mV) (Figure3I-L) and in some cases
189 spiked while SO were suppressed (n= 8/17, 47.05%, mean $_{\text{spiking rate}}$ = 3.03 ± 0.39 spikes/s).
190 This effect was blocked by ketanserin (n = 22) (Figure 3L). We confirmed the presence of 5-
191 HT_{2A}R in Som interneurons using immunohistochemistry in mice expressing EGFP under the
192 5-HT_{2A}R promoter. We found that 11.8 ± 2.9 % of the 5-HT_{2A}R positive cells in EC colocalized
193 with Som (n = 7 mice) (Figure 3–figure supplement 6). These results suggest that Som
194 interneurons might convey synaptic inhibition involved in the suppression of SO.

195 **Som interneurons mediate the suppression of SO by 5-HT**

196 To evaluate the contribution of Som interneurons to the 5-HT-mediated silencing of SO we
197 used an opto- and pharmacogenetic approach. First, we transgenically expressed
198 channelrhodopsin-2 (ChR2) in Som interneurons (Figure 4A). Light-stimulation of ChR2-
199 expressing Som interneurons in vitro suppressed SO consistently (Figure 4D-F). Expectedly,
200 up-states associated spiking was also diminished (Figure 4C, E, F). At the end of the light
201 stimulation spontaneous up-states immediately reoccurred (Figure 4G-H), in line with a critical
202 role of Som interneurons in the modulation of SO (Fanselow et al., 2008, Funk et al., 2017, Niethard
203 et al., 2018). While this experiment establishes the ability of Som interneurons to suppress SO,
204 it does not causally link Som interneuron activation to the suppression of SO induced by 5-
205 HT. Therefore, we generated a transgenic mouse line carrying a Cre-conditional expression
206 cassette of the pharmacogenetic silencer hM4Di (Figure 4–figure supplement 1) (Armbruster et
207 al., 2007). Homozygous Cre-conditional hM4Di transgenic mice and Som-Cre mice were bred
208 to obtain heterozygous Som-Cre/hM4Di offspring, which allow specific inhibition of Som
209 interneuron activity using Clozapine-N-Oxide (CNO). Following application of 5-HT we

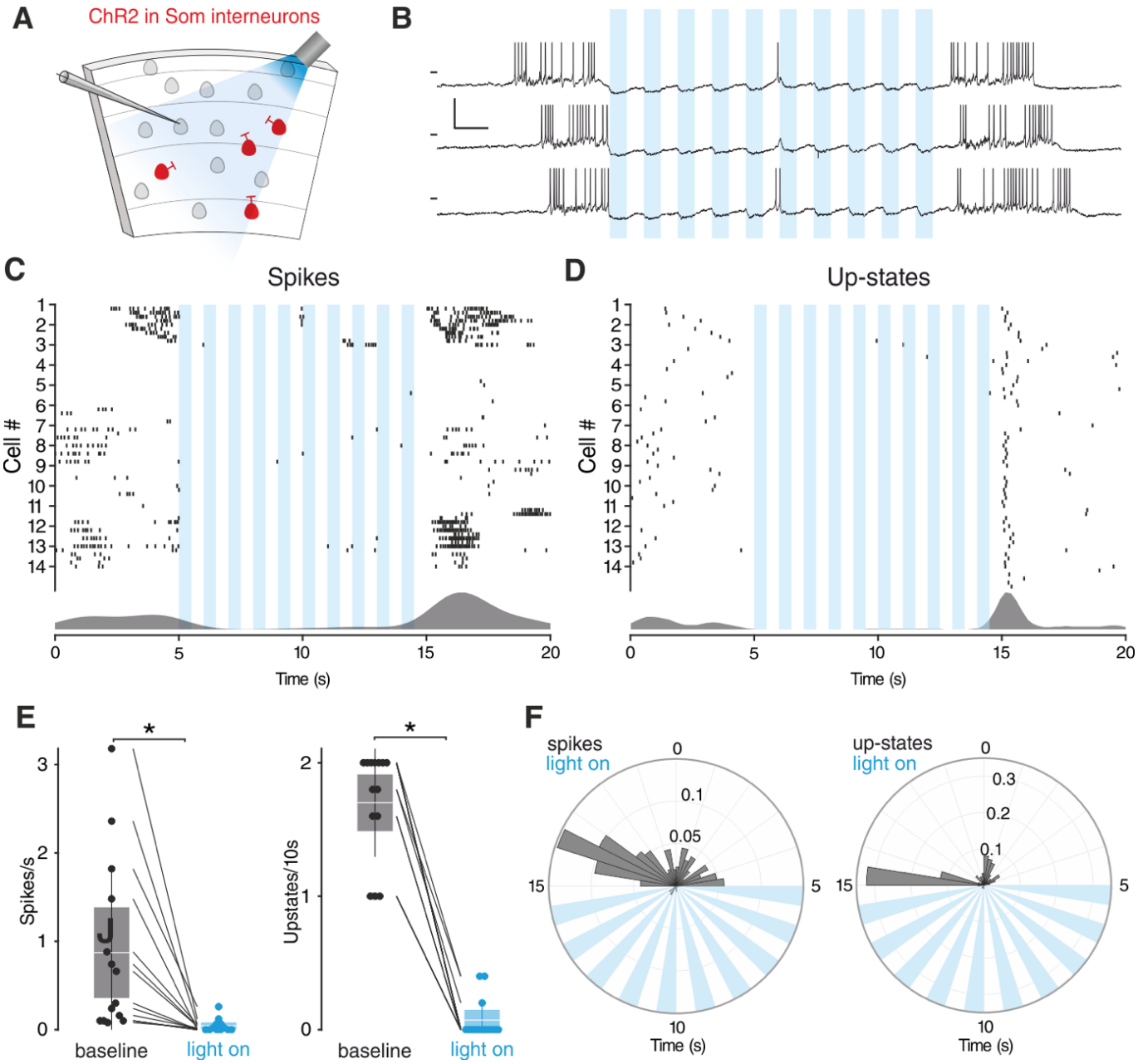

Figure 4| Som interneurons activation suppresses SO. (A) Experimental protocol: Som interneurons expressing ChR2 are activated by light during intracellular recording of layer 3 neurons in EC. (B) Representative recordings from a L3 neuron during Som interneuron activation. Scale bars: 10 mV, 0.5 s. (C) Spikes raster (top) and density plot (bottom) during light stimulation. (D) Up-state raster (top) and density plot (bottom) during light stimulation. (E) Left: spike frequency during baseline light stimulation (n=14; $p < 0.001$, Wilcoxon signed rank test). Right: Up-state incidence during baseline and light stimulation (n=14; $p < 0.001$, Wilcoxon signed rank test). Patches represent 95% confidence interval, lines represent standard deviation. (F) Left: spike probability polar plot during Som interneurons light activation. Right: up-state probability polar plot during Som interneurons light activation. Note the absence of both spiking activity and up-states during Som interneurons activation.

observed a strong reduction of up-state incidence in the LFP, which was partially restored by subsequent application of CNO (Figure 5 A-B). Activation of 5-HT_{1A}R on excitatory cells and the resulting decreased network excitation drive might account for the remaining suppression effect of 5-HT. CNO did not show any significant effect in both wildtype littermates and

hM4Di-PV mice (Figure 5–figure supplement 1), indicative of the specific role played by Som interneurons. In summary, while activation of Som interneurons either via 5-HT or directly by ChR2 suppresses SO, the pharmacogenetic inactivation of Som interneurons weakens the effect of 5-HT on SO.

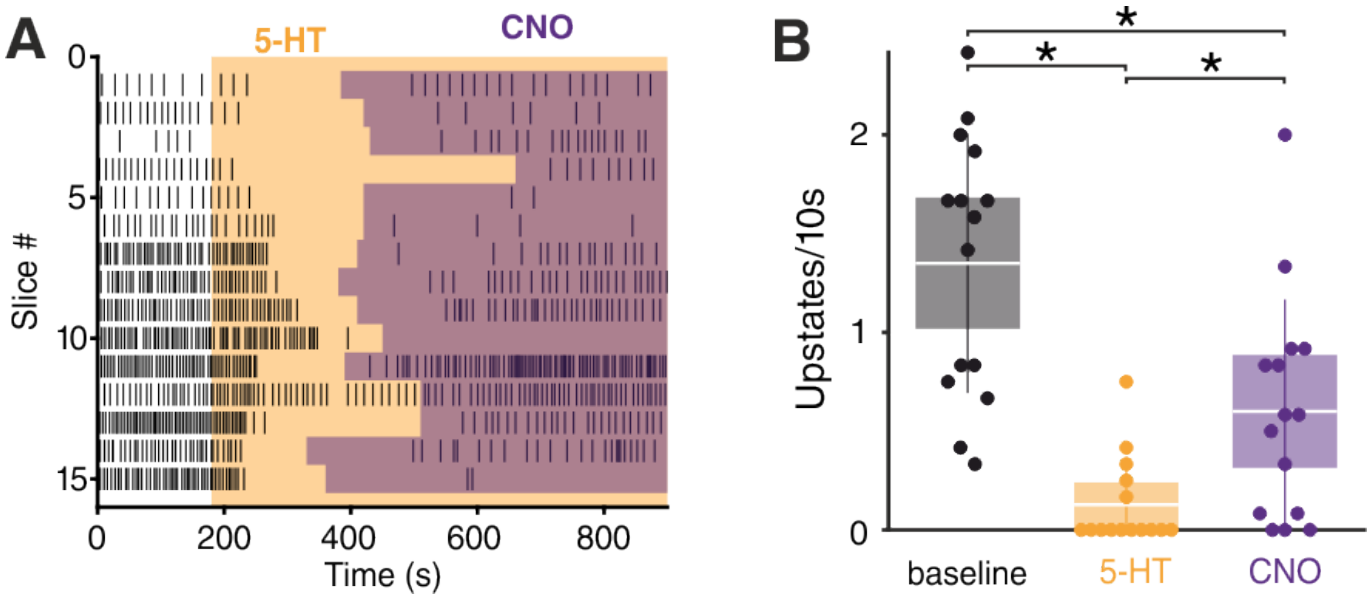

Figure 5| Som interneurons mediate the effect of 5-HT on SO. (A) Up-state raster plot during subsequent 5-HT and CNO application. Orange box represents 5-HT, purple boxes represent CNO. Note the appearance of up-states after CNO application. (B) Up-state incidence during 5-HT and 5-HT+CNO application (n=15; $p_{baseline\ vs\ 5\text{-}HT} < 10^{-4}$, $p_{baseline\ vs\ CNO} = 0.0482$, $p_{5\text{-}HT\ vs\ CNO} = 0.0405$, Kruskal-Wallis test). Patches represent 95% confidence intervals, lines represent standard deviation.

Discussion

In this study we show that 5-HT suppresses default cortical network oscillations and, using an opto- and pharmacogenetic approach, we demonstrate that Som interneurons, activated by 5-HT_{2A}R, mediate this suppression in mEC.

Organization of cortical activity is brain state-dependent, ranging continuously from "synchronized" to "desynchronized" states (Harris and Thiele, 2011). SO is on one end of this continuum, representing the prototypical synchronized state. Our results, in line with previous studies (Puig et al., 2010, Grandjean et al., 2019, Oikonomou et al., 2019), show that 5-HT can suppress synchronized cortical activity; in addition, we identify Som interneurons as necessary for this desynchronization. A parsimonious explanation that links the activation of interneurons and desynchronization relies on tracking of shared input between inhibitory and excitatory populations (Sippy and Yuste, 2013, Renart et al., 2010, Stringer et al., 2016): increased

inhibition, as shown both in computational model and experimental data, can override the effect of shared input causing net decorrelation. Som interneurons, in particular, are known to be sufficient to cause desynchronization in V1 (Chen et al., 2015). While it is well known that Som interneurons are potently excited by acetylcholine (Chen et al., 2015, Obermayer et al., 2018, Fanselow et al., 2008), our work identifies them as a novel target of 5-HT regulation via 5-HT_{2A}R. The excitation of Som Interneurons by 5-HT is likely to contribute to the net inhibitory effect of 5-HT release in many cortical areas (Grandjean et al., 2019, Seillier et al., 2017, Azimi et al., 2020), and could explain why the inhibition strength is linearly correlated to 5-HT_{2A}R expression (Grandjean et al., 2019). Giving further support to this idea, Som interneurons in motor and somatosensory areas show increased cFos levels following 5-HT_{2A}R activation (Martin and Nichols, 2016). Previous works have reported direct 5-HT_{2A}R dependent inhibition in prefrontal cortex (PFC) (Abi-Saab et al., 1999, Ashby et al., 1990, Athilingam et al., 2017), piriform cortex (Marek and Aghajanian, 1994, Sheldon and Aghajanian, 1990), cingulate cortex (Zhou and Hablitz, 1999), cochlear nucleus (Tang and Trussell, 2017), olfactory bulb (Petzold et al., 2009, Hardy et al., 2005), visual cortex (Michaiel et al., 2019, Azimi et al., 2020) and hippocampus (Wyskiel and Andrade, 2016). However, none of these studies identified interneurons using molecular markers and we do not exclude that different interneuron classes in other cortical areas might mediate the inhibitory downstream effects of 5-HT_{2A}R. For example, in PFC a subgroup of PV interneurons has been reported to be activated by this receptor (Athilingam et al., 2017, Puig et al., 2010).

5-HT modulation is also involved in gain regulation. In olfactory cortex, 5-HT has a selective subtractive effect on stimulus evoked firing (Lottem et al., 2016), and a recent work has shown in visual cortex that the reduced gain of evoked responses is dependent on 5-HT_{2A}R activation (Azimi et al., 2020). Intriguingly, Som interneurons have been shown to regulate subtractive inhibition (Sturgill and Isaacson, 2015, Wilson et al., 2012).

Beside its involvement in various physiological brain processes, 5-HT is also associated with the etiology of various psychiatric disorders and the same applies for Som interneurons (Pantazopoulos et al., 2017, Lin and Sibille, 2015). 5-HT is also linked to the psychological effect of many psychotropic drugs. Most interestingly, 5-HT_{2A}R activation is essential for the psychological effects induced by various psychedelics (Nichols, 2016) and, in the case of MDMA, has been linked to perceptual and emotional alterations (Liechti et al., 2000, Kuypers et al., 2018). Broadband reduction in oscillatory power, triggered by 5-HT_{2A}R , seems to be linked to the subjective effect of serotonergic drugs (Carhart-Harris et al., 2016, Carhart-Harris and Friston, 2019) and it has been consistently observed in humans and rodents following

281 administration of MDMA (Frei et al., 2001, Lansbergen et al., 2011) or various other 5-HT_{2A}R
282 agonists (Kometer et al., 2015, Muthukumaraswamy et al., 2013, Carhart-Harris et al., 2016, Wood et
283 al., 2012). The link between 5-HT_{2A}R and perception is further supported by the fact that a
284 number of routinely used antipsychotic drugs are potent 5-HT_{2A}R antagonists (Marek et al.,
285 2003, Meltzer, 1999). While the most recent attempts to explain the psychological effects of 5-
286 HT_{2A}R activation focus on the increased spiking of cortical pyramidal neurons in the deep
287 layers (Carhart-Harris and Friston, 2019, Nichols, 2016), our study suggests that Som interneurons
288 may also play a role. Som interneurons, in contrast to PV interneurons, biasedly form
289 synapses on the dendrites of their target cell (Tremblay et al., 2016). A wealth of evidence
290 suggests that active dendritic processing in cortical pyramidal neurons has a critical influence
291 on sensory perception (Takahashi et al., 2016, Murayama et al., 2009, Smith et al., 2013,
292 Ranganathan et al., 2018) and, in accordance to their unique anatomical properties, Som
293 interneurons strongly influence dendritic computations and directly modulate perceptual
294 thresholds (Takahashi et al., 2016). We propose that the novel link between 5-HT_{2A}R and Som
295 interneurons might help elucidate the mechanism underlying a host of psychiatric disorders
296 and contribute to our understanding of how serotonergic drugs exert their psychological
297 effects.
298

Materials and Methods

All experiments were conducted according to regulations of the Landesamt für Gesundheit und Soziales (Berlin [T 0100/03], Berlin [G0298/18]) and the European legislation (European Directive 2010/63/EU).

Animals

Data for the *in vivo* part of the study were collected from C57BL6 mice (aged 6 to 10 weeks). Data for the *in vitro* part were collected from C57BL6 (P10-P17), Som-tdtomato (P10-P30), Sst-Chr2-EYFP (P10-P16), hM4Di-Som (P10-P15), hM4Di-Som (+/-) (P10-P15) and hM4Di-PV (P10-P15) mice. Immunostainings to localize 5-HT_{2A}R were performed on 5-HT_{2A}R-EGFP mice (P20-P90) and Immunostainings to localize 5-HT fibers (Fig.1 c) were performed on an ePet-YFP mouse (P35). The animals were housed in a 12:12 hours light-dark cycle in singularly ventilated cages with *ad libitum* access to food and water. SO *in vitro* recordings were performed on P12-P16 mice.

Drugs

Urethane (U2500, Sigma), fenfluramine ((+)-Fenfluramine hydrochloride, F112, Sigma), 5-HT (Serotonin creatinine sulfate monohydrate, H7752, Sigma), WAY-100635 (W108, Sigma), α-Methylserotonin (α-Methylserotonin maleate salt, M110, Sigma) MDMA ((±)3,4-methylenedioxymethamphetamine, 64057-70-1, Sigma), CNO (Clozapine *N*-oxide dihydrochloride, 6329, Tocris) were dissolved in water for *in vitro* application and in 0.9% normal saline for *in vivo* application. Ketanserin (Ketanserin (+)-tartrate salt, S006, Sigma) was dissolved in Dimethyl sulfoxide (DMSO).

Surgery and *in vivo* recording

Mice were briefly anaesthetized with isofluorane (2%) and then injected intraperitoneally with urethane (1,2 g/kg, Sigma Aldrich, Munich, Germany). The level of anesthesia was maintained so that hindlimb pinching produced no reflex movement and supplemental doses of urethane (0.2 g/kg) were delivered as needed. Upon cessation of reflexes the animals were mounted on a stereotaxic frame (Kopf Instruments, Tujunga, California), and body temperature was maintained at 38°C. The scalp was removed, and the skull was cleaned with saline solution. A craniotomy was performed at +3 mm ML, -3 mm AP, +3.25 mm DV.

Extracellular recordings from EC were performed using a Cambridge Neurotech 64-channels (n = 15) or 32-channels (n = 3) silicon probe. The recording electrode was painted with the fluorescent dye DiI (Thermo Fisher Scientific, Schwerte, Germany) and then slowly lowered into the craniotomy using micromanipulators (Luigs&Neumann, Ratingen, Germany) at a 25° angle AP (toward the posterior side of the brain). The exposed brain was kept moist using saline solution. A ground wire connected to the amplifier was placed in the saline solution covering the skull to eliminate noise. Brain signals were recorded using a RHD2000 data acquisition system (Intan Technologies, Los Angeles, California) and sampled at 20kHz. Recording quality was inspected on-line using the open-source RHD2000 Interface Software. Recordings began after a 10-minute waiting period in which clear Up-states could consistently be seen at a regular frequency.

In vivo **analysis**

We selected the channel to use for up-state detection based on the standard deviation (STD) of the trace during baseline (first 5 minutes of recording), the channel with the highest STD was selected as larger voltage deflection increases detection algorithm accuracy. Given the highly synchronous nature of SO (Supplementary Fig. 3) the spatial location of the channel selected was not considered. Up-states were detected comparing threshold crossing points in two signals: the delta-band filtered signal (0.5-4 Hz) and the population spike activity. Candidate up-states were identified in the delta-band filtered signal using two dynamic thresholds ‘a’ and ‘b’:

$$a = m + \frac{\sigma}{1.5}$$

$$b = m + \frac{\sigma}{0.8}$$

Where σ is the standard deviation of the signal during the first five minutes of recording (baseline) and *m* is the centered moving median calculated using 60 s windows (Matlab function *movmedian*). The median was used instead of the mean to account for non-stationaries in the data. A candidate up-state was identified at first using the threshold crossings of the signal compared to ‘a’: candidates shorter than 200 ms were deleted and candidates happening in a window of 300 ms were joined together. Subsequently the threshold ‘b’ was used to separate up-states occurring in close proximity: if the signal within one candidate crossed the threshold ‘b’ in more than one point then the candidate up-state was split in two at the midpoint between the two threshold crossings. Candidate up-states

were finally confirmed if the population spike activity (calculated in 100 ms windows) within the candidate crossed a threshold of 1 σ (calculated during the baseline).

Units detection and classification

Spike detection was performed offline using the template-based algorithm Kilosort2 (https://github.com/MouseLand/Kilosort2), with the following parameters:

- ops.fshigh = 300
- ops.fsslow = 8000
- ops.minfr_goodchannels = 0
- ops.Th = [8 4]
- ops.lam = 10
- ops.AUCsplit = 0.9
- ops.minFR = 1/1000
- ops.momentum = [20 400]
- ops.sigmaMask = 30
- ops.ThPre = 8
- ops.spkTh = -6
- ops.nfilt_factor = 8
- ops.loc_range = [3 1]
- ops.criterionNoiseChannel = 0.2
- ops.whiteningrange = 32
- ops.ntbuff = 64

Manual curation of the results was performed using Phy (https://github.com/cortex-lab/phy). Each Isolated unit satisfied the following two criteria: Refractory period (2 ms) violations < 5%, fraction of spikes below detection threshold (as estimated by a gaussian fit to the distribution of the spike amplitudes) < 15%. Units with negative maximal waveform amplitude were further classified as putative excitatory if the latency (TP latency) was 0.55 ms or putative inhibitory when TP latency < 0.55 ms. The value 0.55 was chosen in accordance with previous works (Senzai et al., 2019, Antoine et al., 2019). Pharmacological classification: units were classified as 'activated' if their firing rate in the 25 minutes following drug injection was 2 σ (standard deviation) above the baseline rate for at least 5 minutes. Remaining units were pulled together in the category 'non-activated'.

Cross-correlogram analysis

Cross-correlogram based connectivity analysis was performed for every unit to identify inhibitory connections. Units with a spiking rate smaller than 0.3 spikes/s were discarded from the analysis. We used total spiking probability edges (TPSE) algorithm (https://github.com/biomemsLAB/TSPE) (De Blasi et al., 2019) to identify in a computationally efficient manner putative inhibitory connections between units and all clusters recorded. The parameters used were:

- d = 0,
- neg_wins = [2, 3, 4, 5, 6, 7, 8],
- co_wins = 0,
- pos_wins = [2, 3, 4, 5, 6],
- FLAG_NORM = 1.

The connectivity vectors of each unit resulting from TSPE were sorted by inhibition strength. Top 20 connections were further analyzed using custom Matlab code. A connection was classified as inhibitory if the cross correlogram values (x) were smaller than the mean of x by more than one standard deviation ($x < mean(x) - std(x)$) in at least 4 consecutive bins (bin size = 1 ms) in a window 4 to 9 ms after the center of the cross-correlogram.

Slice preparation

We prepared acute near horizontal slices (~15° off the horizontal plane) of the medial entorhinal cortex (mEC) from C57Bl6/n mice. Animals were decapitated following isoflurane anesthesia. The brains were quickly removed and placed in ice-cold (~4° C) ACSF (pH 7.4) containing (in mM) 85 NaCl, 25 $NaHCO_3$, 75 Sucrose, 10 Glucose, 2.5 KCl, 1.25 NaH_2PO_4, 3.5$MgSO_4$, 0.5 $CaCl_2$, and aerated with 95% O_2, 5% CO_2. Tissue blocks containing the brain region of interest were mounted on a vibratome (Leica VT 1200, Leica Microsystems), cut at 400 µm thickness, and incubated at 35 °C for 30 min. The slices were then transferred to ACSF containing (in mM) 85 NaCl, 25 $NaHCO_3$, 75 Sucrose, 10 Glucose, 2.5 KCl, 1.25 NaH_2PO_4, 3.5 $MgSO_4$, 0.5 $CaCl_2$. The slices were stored at room temperature in a submerged chamber for 1-5 hr before being transferred to the recording chamber.

In vitro recording

In order to perform whole-cell recordings slices were transferred to a submersion style recording chamber located on the stage of an upright, fixed-stage microscope (BX51WI, Olympus) equipped with a water immersion objective (×60, Olympus) and a near-infrared charge-coupled device (CCD) camera. The slices were perfused with ACSF (~35 °C bubbled with 95 % O2-5 % CO2) at 3-5 ml/ min to maintain neuronal health throughout the slice. The ACSF had the same composition as the incubation solution except for the concentrations of calcium and magnesium, which were reduced to 1.2 and 1.0 mM, respectively. Recording electrodes with impedance of 3-5 MΩ were pulled from borosilicate glass capillaries (Harvard Apparatus, Kent, UK; 1.5 mm OD) using a micropipette electrode puller (DMZ Universal Puller). The intracellular solution contained the following (in mM): 135 K-gluconate, 6 KCl, 2 MgCl2, 0.2 EGTA, 5 Na2- phosphocreatine, 2 Na2-ATP, 0.5 Na2-GTP, 10 HEPES buffer, and 0.2% biocytin. The pH was adjusted to 7.2 with KOH. Recordings were performed using Multiclamp 700A/B amplifiers (Molecular Devices, San Jose, California). The seal resistance was >1 GΩ. Capacitance compensation was maximal and bridge balance adjusted. Access resistance was constantly monitored. Signals were filtered at 6 kHz, sampled at 20 kHz, and digitized using the Digidata 1550 and pClamp 10 (Molecular Devices, San Jose, California). Activation light was delivered by a 460 nm laser (DPSS lasers, Santa Clara, California) using a 460–480 nm bandpass excitation filter. Stimulation consisted of 500 ms pulses at 1 Hz.

Stimulation experiments were performed using a bipolar micro-electrode (glass pipette filled with ACSF solution, wrapped by a fine grounding wire) connected to an isolated voltage stimulator (ISO-Flex, A.M.P.I., Israel). A 4x objective (Olympus) was used to visually guide the stimulating electrode into the mEC. Stimulation power was adjusted to achieve consistent up-state generation during baseline (> 95%). Each stimulus had a duration of 50 μs, inter-stimuli interval was 8-10 seconds.

In vitro analysis

In vitro up-states were detected in Matlab using an algorithm similar to the one described in the *in vivo analysis* method section. We used a coincident detection in two signals. In multicellular recordings we used the membrane potential of 2 cells, in single cell recording we used membrane potential and the envelope of the gamma filtered trace (50-250 Hz), as up-states are characterized by an increase in gamma activity (Neske, 2015).

Baseline condition was calculated using the last 120 s before drug application, post-drug application condition was calculated using the last 120 s of recording after drug application (Total recording duration: 600 s).

Excitatory (Exc), fast spiking (FS) and low-threshold spiking (LTS) neurons were classified using Gaussian mixture models (GMM) with a soft clustering approach in Matlab. Input resistance (R_{in}), Δafter-hyperpolarization (ΔAHP), sag, rheobase, spike width and resting potential (RP) were extracted from each neuron and used in the classification. The first two components of the principal component analysis (PCA) were used to fit the data to a Gaussian mixture model distribution. Initial values were set according to the k-means algorithm with centroid positioned at x and y position: 5, 0; -15, -15; -15, 10. This centroid were placed according to the loadings of the PCA to identify 3 clusters with the following main features:

- Cluster 1 (putative Exc): high spike width, low AHP, low rheobase.
- Cluster 2 (putative FS): low spike width, low SAG, high rheobase, low R_{in}.
- Cluster 3 (putative LTS): low spike width, high SAG, high AHP, high R_{in}.

Covariance matrices were diagonal and not shared. Neurons with a posterior probability of belongings to any of the three clusters < 90% were discarded from further analysis (1/49). While the majority of Som-interneurons display LTS features, a minority (~10%) belongs to the FS group (Urban-Ciecko et al., 2015). To distinguish FS and LTS interneurons in the SOM-Td Tomato mice we employed the GMM with posterior probability threshold of 90%.

Inter-area connectivity analysis

Projection data was downloaded from the from the Allen Mouse Brain Connectivity Atlas via the provided API (application programming interface) using freely available code (https://github.com/SainsburyWellcomeCentre/AllenBrainAPI). Different connectivity metrics are provided for each experiment:

- Normalized projection volume = $\frac{\text{Projection volume}}{\text{Total volume of signal in injection site}}$
- Projection density = $\frac{\text{Number of pixels identified as projecting in the structure}}{\text{Number of valid pixels in the structure}}$
- Projection intensity = $\frac{\text{Sum of intensity values in projecting pixels in the structure}}{\text{Number of pixels identified as projecting in the structure}}$
- Projection energy = $\frac{\text{Projection density}}{\text{projection intensity}}$

We chose to use projection energy as it directly relates signal strength (pixel intensity) to the size of a give structure (total number of pixels in the structure), in this case a widely spread

weak signal and a narrow strong signal may both have similar projection energies. Projection energy was normalized across different experiments dividing by the injection volume. Projection signal in injection area was excluded. More information about the record properties can be found on the Allen SDK (software development kit) website https://alleninstitute.github.io/AllenSDK/unionizes.html. Each annotation was assigned a new additional structure ID to enable the calculation of average projection energy per area. Entorhinal cortex (EC) output was calculated combining the results of experiments 114472145 (injection site: lateral EC) and 113226232 (injection site: medial EC).

Connectivity analysis was performed using custom Matlab (2018a) code, the code is available on Github (https://github.com/RobertoDF/BRIO).

Generation of Cre-conditional hM4Di mice

We produced a transgenic mouse line carrying a Cre-conditional hM4Di expression cassette in the Rosa26 locus. The transgene construct was inserted by recombination-mediated cassette exchange (RMCE). RMCE relies on recombination events between attB and attP recognition sites of the RMCE plasmid and genetically modified acceptor embryonic stem (ES) cells, mediated by the integrase of phage phiC31(Hitz et al., 2007). The RMCE construct is thereby shuttled into the Rosa26 locus of the ES cells, along with a Neomycin resistance cassette (fig. S12A). The acceptor cell line IDG3.2-R26.10-3 (I3) was kindly provided by Ralf Kühn (GSF National Research Centre for Environment and Health, Institute of Developmental Genetics, Neuherberg, Germany).

We subcloned a Cre-conditional FLEX (flip-excision) cassette (Schnutgen et al., 2003) into pRMCE, and inserted a strong CAG promoter (CMV immediate early enhancer/modified chicken β-actin promoter, from Addgene Plasmid #1378) in front of the FLEX-cassette to create pRMCE-CAG-Flex. The coding sequence of hM4Di-mKateT was inserted into the FLEX cassette in reverse orientation to the promoter (fig. S12A). Finally, a rabbit globulin polyA cassette including stop codons in every reading frame was placed downstream of the FLEX cassette, in the same direction as hM4Di, in order to prevent unintended transcriptional read-through from potential endogenous promoters. The construct was completely sequenced before ES cell electroporation.

Electroporation of the RMCE construct together with a plasmid encoding C31int was performed by the transgene facility of the 'Research Institute for Experimental Medicine' (FEM, Charité, Berlin) according to published protocols (Hitz et al., 2009, Hitz et al., 2007).Recombinant clones were selected by incubation with 140 µg/ml G418 for at least 7 days. To activate hM4Di

expression by recombination of the FLEX switch, selected clones were further transfected transiently with pCAG-Cre-EGFP using Roti-Fect (Carl Roth, Karlsruhe, Germany). G418-resistant clones were analyzed by PCR for successful integration and recombination of the construct (fig. S12B), using the following primer:
GT001 PGK3'-fw: CACGCTTCAAAAGCGCACGTCTG;
GT002 Neo5'-rev: GTTGTGCCCAGTCATAGCCGAATAG;
GT005 PolyA-fw: TTCCTCCTCTCCTGACTACTCC;
GT006 Rosa3'-rev: TAAGCCTGCCCAGAAGACTC;
GT013 hM4Di3'rec-rev: CAGATACTGCGACCTCCCTA
After verification of correct integration and functional FLEX-switch recombination, we generated chimeras by blastocyst injection of I3 ES cells. Heterozygous offsprings were mated with a Flpe deleter mouse line in order to remove the neomycin resistance cassette by Flp-mediated recombination.
Mice homozygous for the Rosa-CAG-FLEX-hM4Di-mKateT allele are viable and fertile and show now obvious phenotype. Importantly, application of CNO to these mice does not induce any behavioral effects. Homozygous Cre-conditional hM4Di transgenic mice and Som-Cre mice (Taniguchi et al., 2011) were maintained on a C57BL/6n genetic background and were bred to obtain heterozygous Som-Cre / hM4Di offsprings.

Histological analysis

For the *post-mortem* electrode tracks reconstructions of the *in vivo* recordings, mice were not perfused, brain were extracted from the skull, post-fixed in 4% PFA overnight at 4°C and afterwards cut with a vibratome (Leica Microsystems, Wetzlar Germany) in 100 µM thick sequential sagittal slices. Images were taken using a 1.25x objective and stitched together using the microscope software (BX61, Olympus), afterwards we used AllenCCF code (https://github.com/cortex-lab/allenCCF) to identify electrode shanks location (Shamash et al., 2018).
For the anatomical reconstructions of recorded cells *in vitro* brain slices were fixed with 4% paraformaldehyde in 0.1 M phosphate buffer (PB) for at least 24 hours at 4°C. After being washed three times in 0.1 M PBS, slices were then incubated in PBS containing 1% Triton X-100 and 5% normal goat serum for 4 hr at room temperature (RT). To visualize biocytin-filled cells we used Streptavidin Alexa 488 conjugate (1:500, Invitrogen), WFS1 (1:1000, Rabbit, Proteintech, IL, USA) was used in a subset of analysis to visualize the L2/L3 border, Som (1:1000, Rat, Bachem, Switzerland) was used in the 5-HT_{2A}R localization analysis. Slices were

incubated with primary antibodies for 48 hours at RT. After rinsing two times in PBS, sections were incubated in the PBS solution containing 0.5% Triton X-100, Alexa fluor 488, Alexa fluor 555 and Alexa fluor 647 (Invitrogen Corporation, Carlsbad, CA) according to the number of antibodies used. Slices were mounted in Fluoroshield (Sigma-Aldrich) under coverslips 2-3 hr after incubation with the secondary antibodies and stored at 4 °C.

Labeled cells were visualized using 20x or 40x objectives on a confocal microscope system (SP8, Leica). For the 5-HT_{2A}R localization analysis images of the whole EC were acquired and stitched together using the auto stitching method, with smoothing set to off. Z stacks were acquired every 30 µM. The Image stacks obtained were registered and combined in Fiji (http://fiji.sc/wiki/index.php/Fiji) to form a montage of the sections. Cell counting was executed using Fiji multi-point tool. X-Y-Z coordinates of each 5-HT_{2A}R-EGFP positive cell were exported to Matlab and subsequently, using custom written code in Matlab, we semi-automatically inspected each cell for colocalization between EGFP(5-HT_{2A}R) and Som.

Statistical Analysis

All datasets were tested to determine normality of the distribution either using D'Agostino-Pearson omnibus normality test or Shapiro-Wilk normality test. Student's t-test and one-way ANOVA were used for testing mean differences in normally distributed data. Wilcoxon matched-pairs signed rank test and Kruskal-Wallis were used for non-normally distributed datasets. Dunn-Sidak multiple comparison test was used to compare datasets with 3 or more groups. Kolmogorov-Smirnov test was used to compare cumulative distributions. Statistical analysis was performed using Prism (6.01) and Matlab (2019a).

All data are expressed as mean ± SEM Asterisks in figures represents p-values smaller than 0.05 unless stated otherwise in the legend.

Data and code availability

The code generated during this study is available from the corresponding author upon reasonable request.

Acknowledgments: We thank A. Schönherr, S. Rieckmann, K. Czieselzky, A. Fortströer, A.R. Sammons, M. Brecht, M. E. Larkum.

Author contributions: Conceptualization: R.D.F. and D.S.. Methodology: J.J.T., P.B., R.D.F and B.R.. Investigation: R.D.F, A.S., C.C. and P.B. Software and formal analysis: R.D.F..

579 Resources: P.B. and C.H.. Supervision: D.S.. Project administration: R.D.F., D.S.. Funding
580 acquisition: D.S.. Original draft preparation: R.D.F. and D.S. Review and editing: all authors.
581

Supplementary Figures

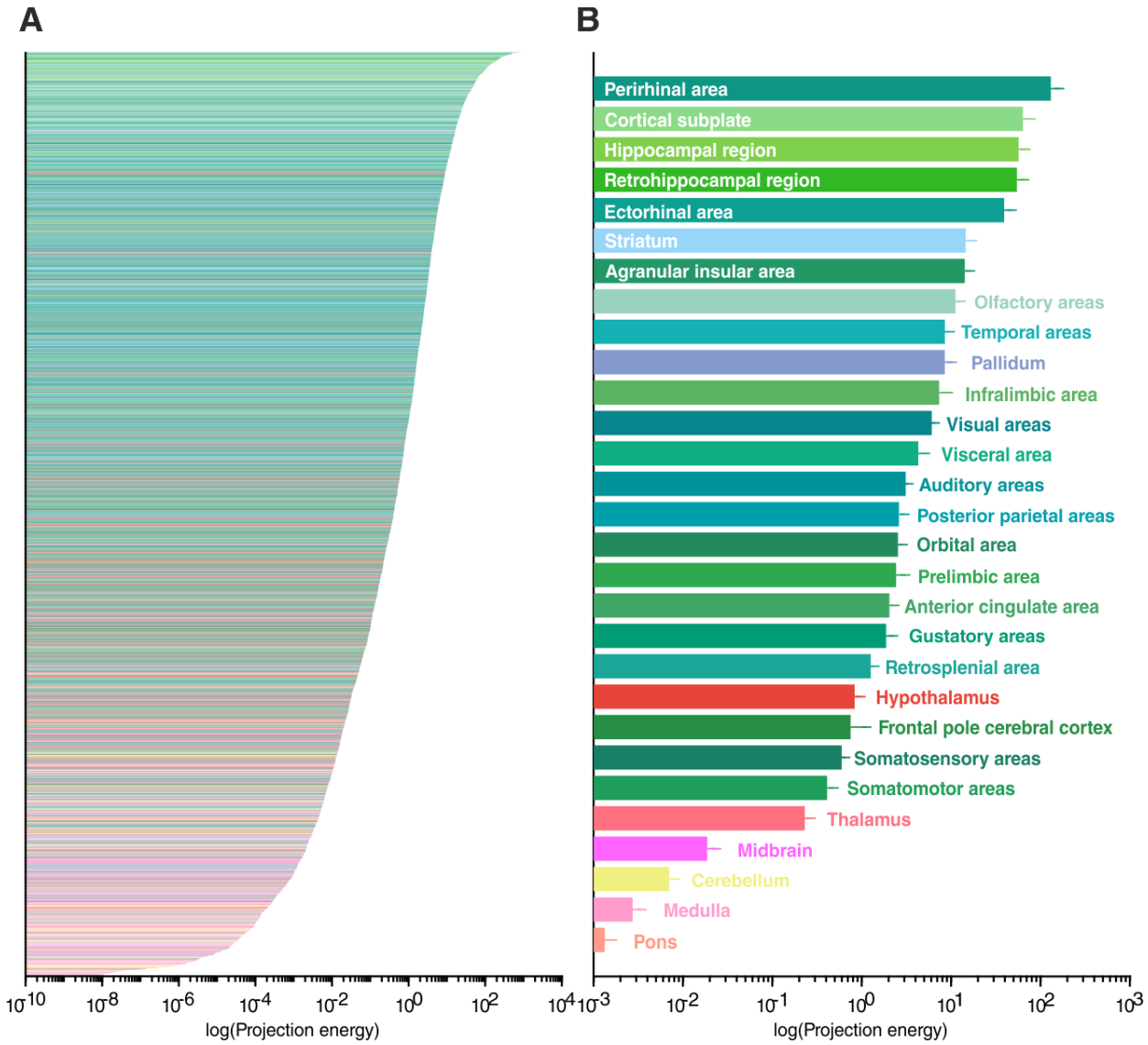

Figure 1–figure supplement 1. Regional output connectivity of EC.
(A) Projection energy of all identified EC outputs color coded according to Allen institute standard: green = cerebral cortex, blue= cerebral nuclei, pink = midbrain, red = interbrain/hindbrain and yellow = cerebellum. **(B)** Same data as (A) consolidated in higher level regions.

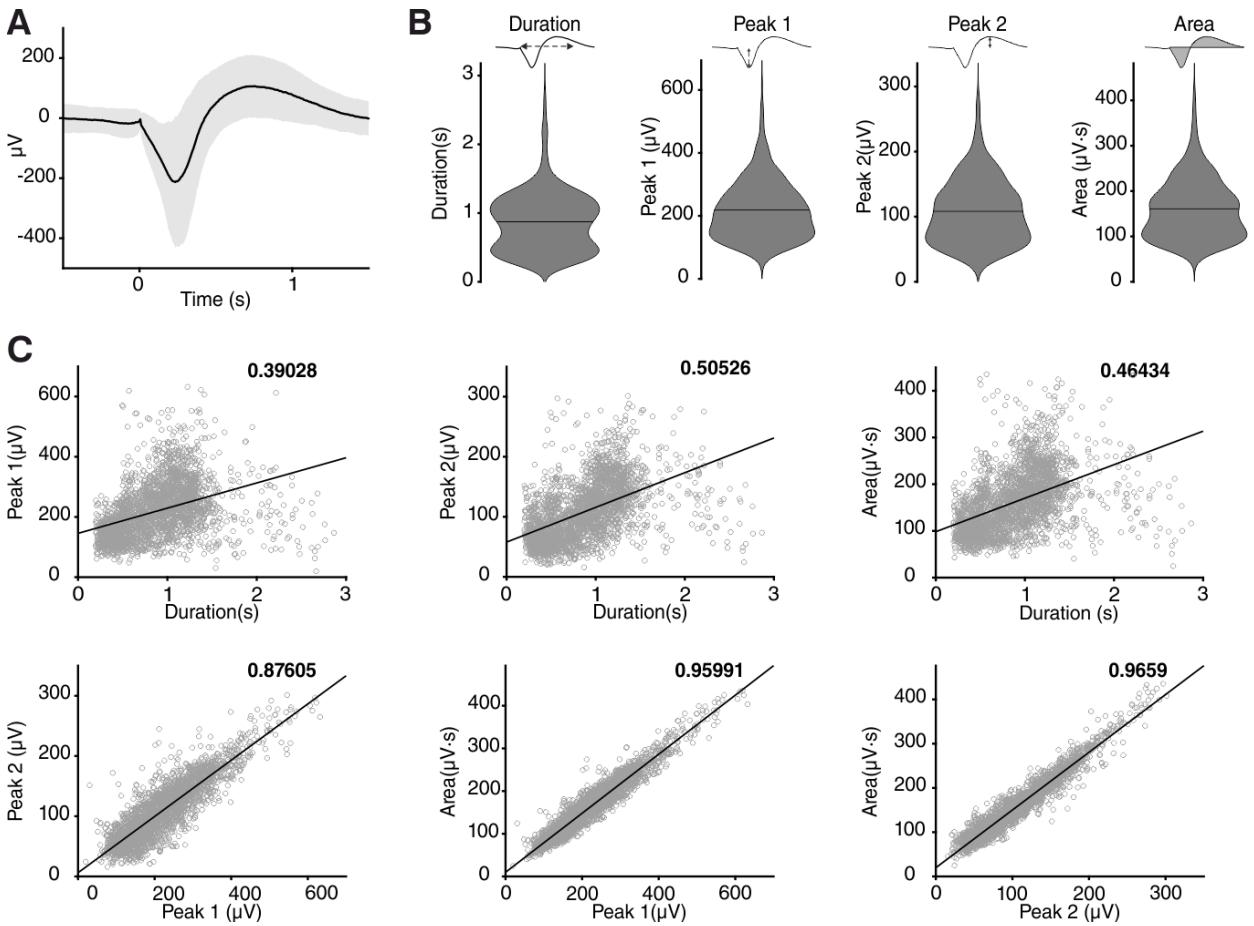

Figure 1–figure supplement 2. *In vivo* up-state metrics.

(A) Average up-state voltage deflection, grey patch represents 1 standard deviation ($n_{detected\ up\text{-}states} = 2655$, $n_{animals} = 18$). For each recording the channel with the biggest voltage deflection was selected, see "Methods". For experiments with drug application (either MDMA or Fen) only baseline up-states were taken in account. **(B)** Violin plots of duration (mean: 0.87 ± 0.008 s), peak 1 amplitude (mean: 218.59 ± 1.83 μV), peak 2 amplitude (mean: 108.27 ± 0.97 μV) and area (mean: 160.88 ± 1.31 μV·s) of each detected up-state. **(C)** Scatter plots showing relationships between metrics used in (B). Bold black number in each plot represent the correlation coefficient ($p < 0.001$).

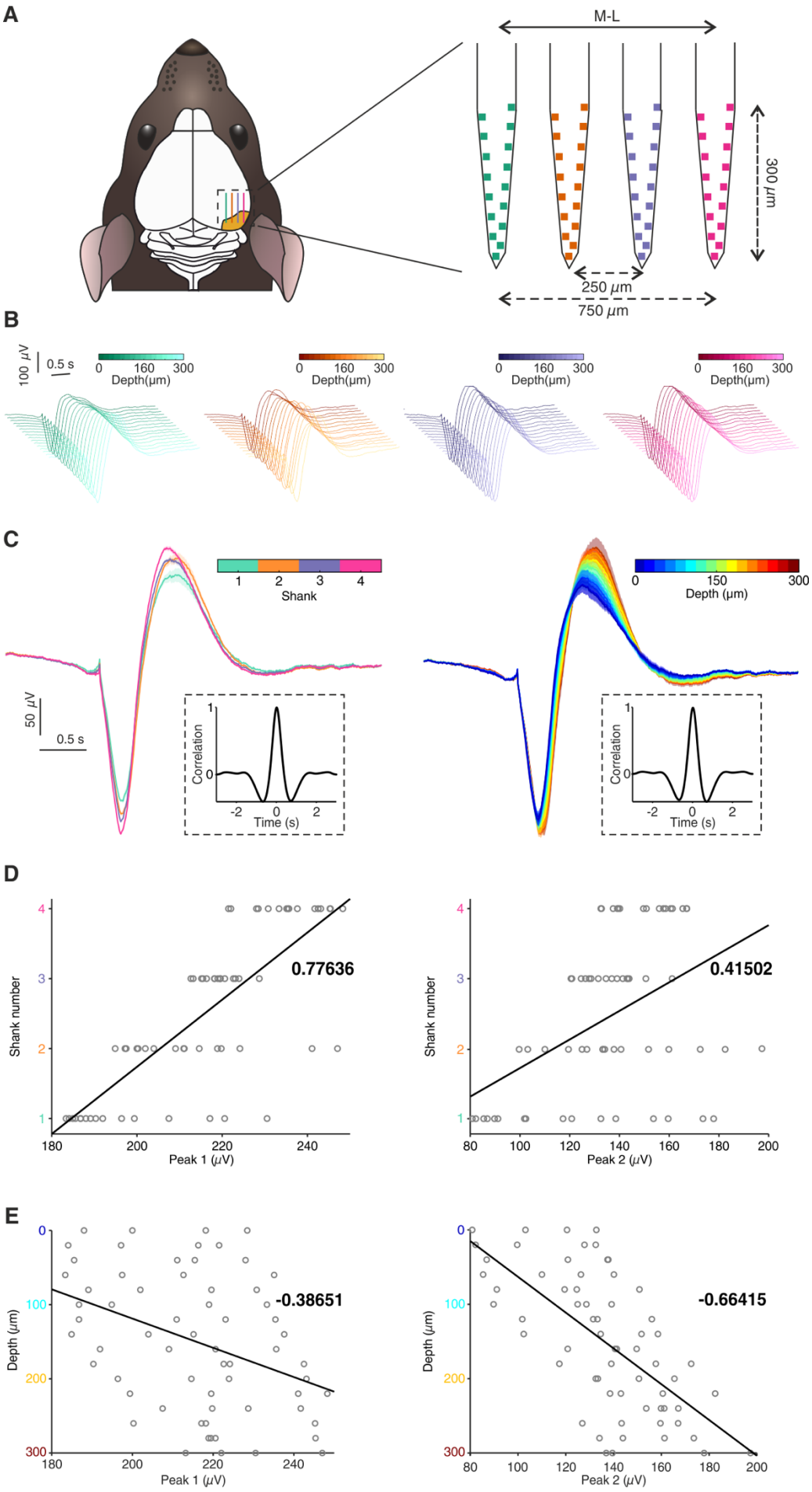

599 **Figure 1–figure supplement 3. *In vivo* up-state spatial features.**

(A) Microelectrode implant location and microelectrode features. 64 channels ($n_{animals}$= 15, n_{shanks} = 4) and 32 channels ($n_{animals}$ = 3, n_{shanks} = 2) microelectrodes were used in this study, analysis shown in this figure excludes data recorded with 32 channels probe due to the different spatial configuration of the channels. **(B)** Average up-state voltage deflection for each channel of the microelectrode. For experiments with drug application (either MDMA or Fen) only baseline up-states were taken in account. **(C)** Left: Average up-state voltage deflection grouped by shank. Right: Average up-state voltage deflection grouped by depths (right). Insets show the normalized correlation between averages in the two different groups. **(D)** Scatter plots showing significant correlation between shank number and peak 1 (left) and between shank number and peak 1 (right). Bold black number in each plot represent the correlation coefficient ($p < 0.001$). **(E)** Scatter plots showing significant correlation between recording channel depth and peak 1 (left) and between recording channel depth and peak 1 (right). Bold black number in each plot represent the correlation coefficient ($p < 0.001$).

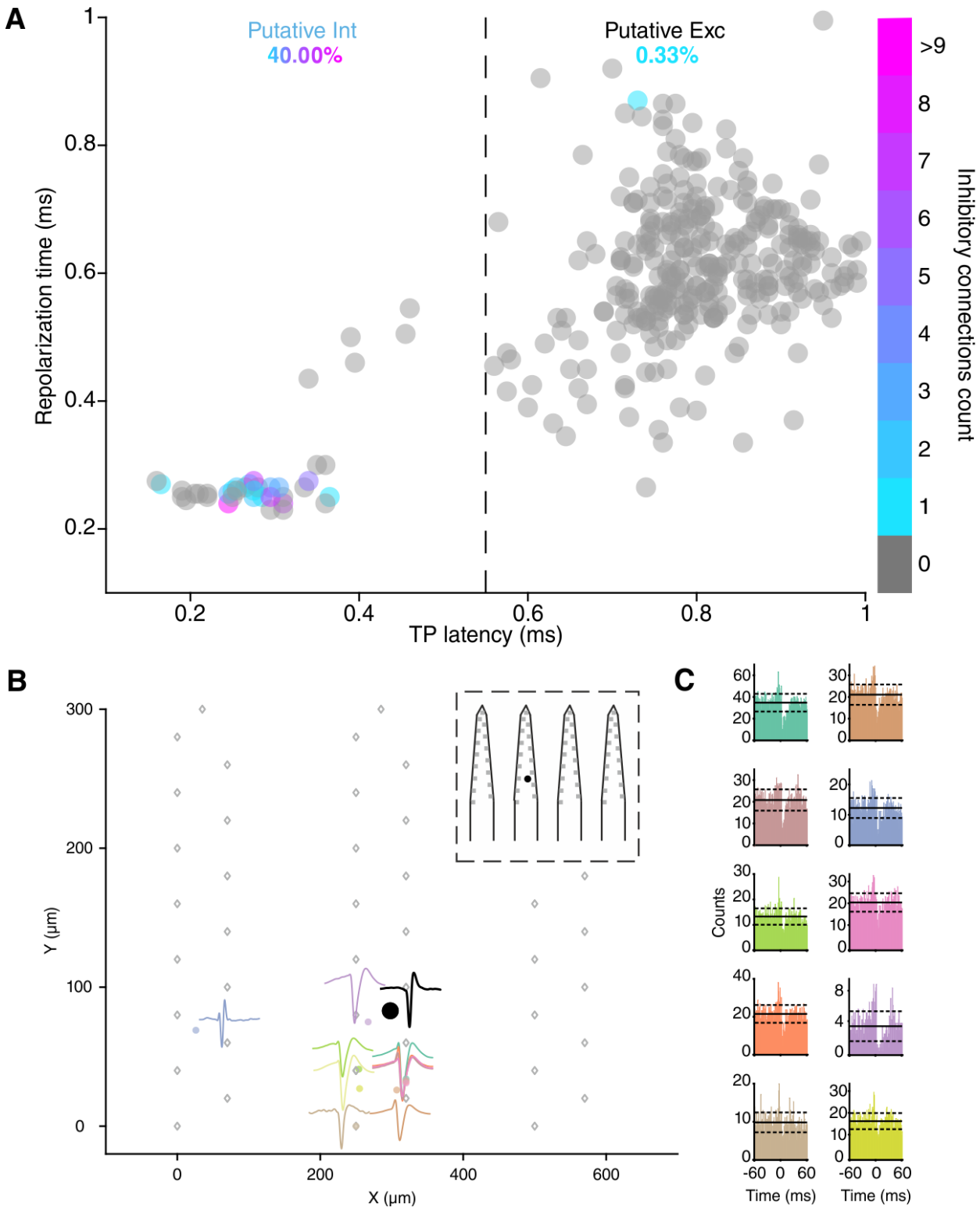

Figure 2–figure supplement 1. Cross-correlogram (CCG) based connectivity analysis. **(A)** Units are plotted according to TP latencies and repolarization time and color-coded according to the number of inhibitory connections detected. Units displaying a TP latency < 0.55 ms were classified as putative inhibitory interneurons ('Putative int'), the remaining units were classified as putative excitatory neurons ('Putative exc'). Inhibitory connections were detected using Total Spiking Probability Edges (TSPE) (See Supplementary materials). Putative interneurons had a 40.0 % chance of displaying at least one inhibitory connection in the CCGs with an average number of 3.38 ± 0.68 inhibitory connections while putative excitatory cells had a 0.33 % chance of displaying inhibitory connections. **(B)** Connectivity

scheme of one putative inhibitory unit (source unit, black circle) displaying 10 inhibitory connections with surrounding clusters. Grey rhombi represent recording channels on the probe with the tip of the shanks pointing north. Each colored circle represents the location of an inhibited unit. Waveforms of the inhibited units are plotted nearby the location using the same color. Inset shows the location of the source unit on the probe. **(C)** CCGs of the connections displayed in (B) using the same color code. Solid lines represent mean, dashed lines represent 1 standard deviation.

A

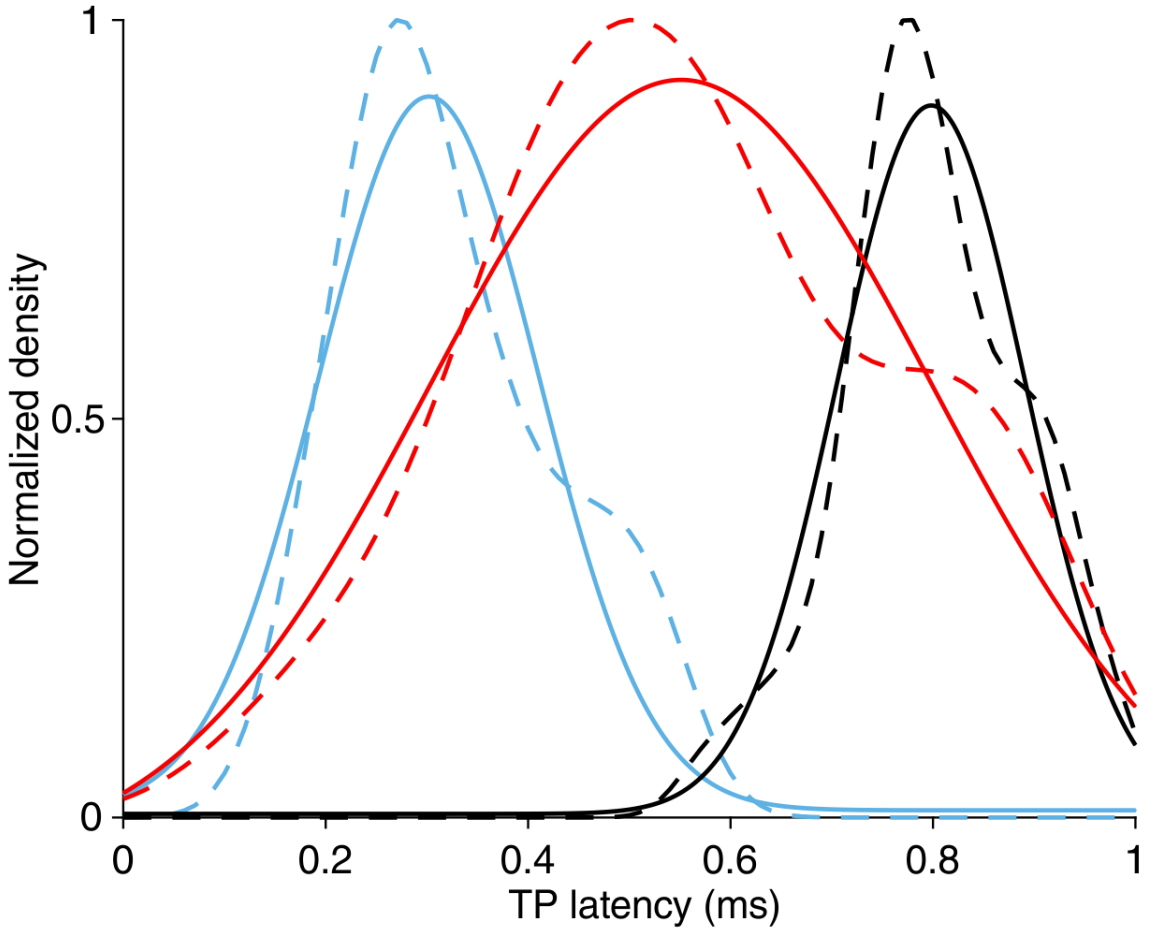

B

Gof metrics	Excitatory	Inhibitory	Activated
sse	0.6764	0.3036	0.5860
rsquare	0.9340	0.9669	0.9353
dfe	97	97	97
adjrsquare	0.9320	0.9659	0.9333

Figure 2–figure supplement 2. TP latency density distributions.
(A) Dashed lines represent kernel density estimations of probability density functions of the TP latencies of putative inhibitory (blue), putative excitatory (black) and 'activated' units. Solid lines represent gaussian fitting curves for each group. Peak inhibitory gaussian: 0.31 ms, peak excitatory gaussian: 0.81 ms and peak 'activated' gaussian: 0.56 ms. **(B)** Goodness of fit metrics for each gaussian fit. Sse = Sum of squares due to error, rsquare = R-squared (coefficient of determination), dfe = Degrees of freedom in the error, adjrsquare = Degree-of-freedom adjusted coefficient of determination.

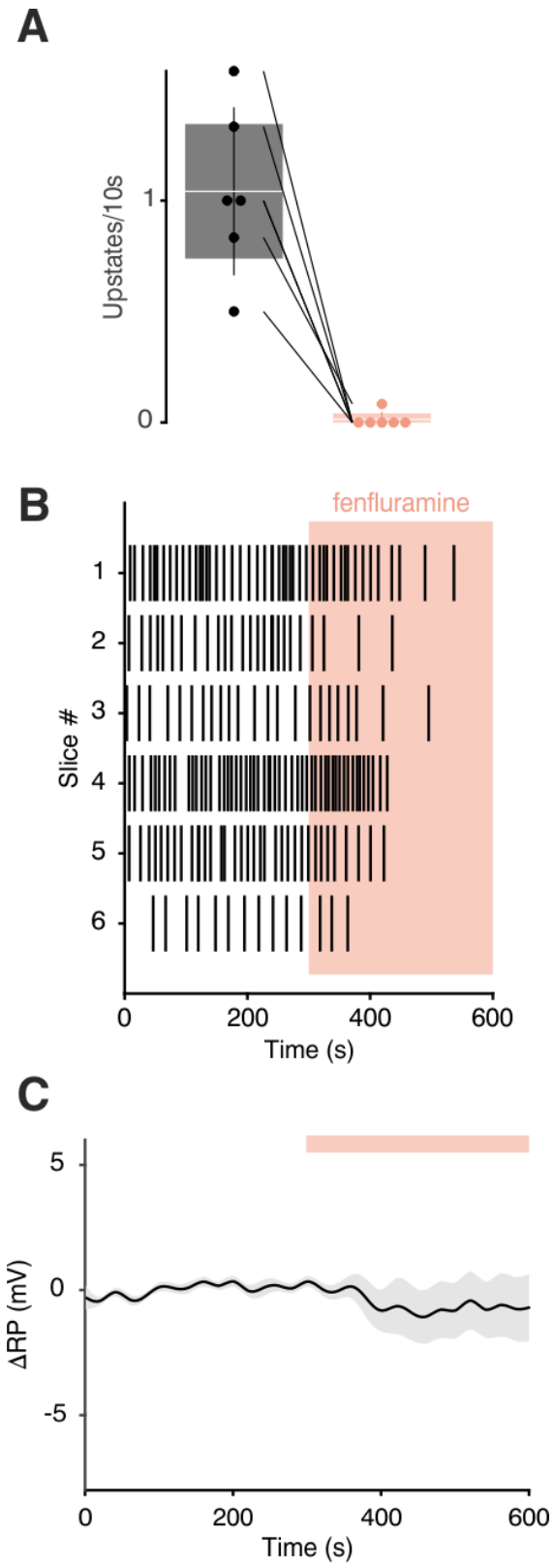

Figure 3–figure supplement 1. Effect of fenfluramine on SO.
(A) Histogram of UDS incidence before and after fenfluramine application (n= 6, baseline: 1.04 ± 0.15 Up-states/10s, fenfluramine: 0.01 ± 0.01 Up-states/10s). **(B)** Up-state raster plot during fenfluramine application. **(C)** Change in resting potential (RP) after fenfluramine application (n=13, ΔRP = -0.70 ± 1.17 mV).

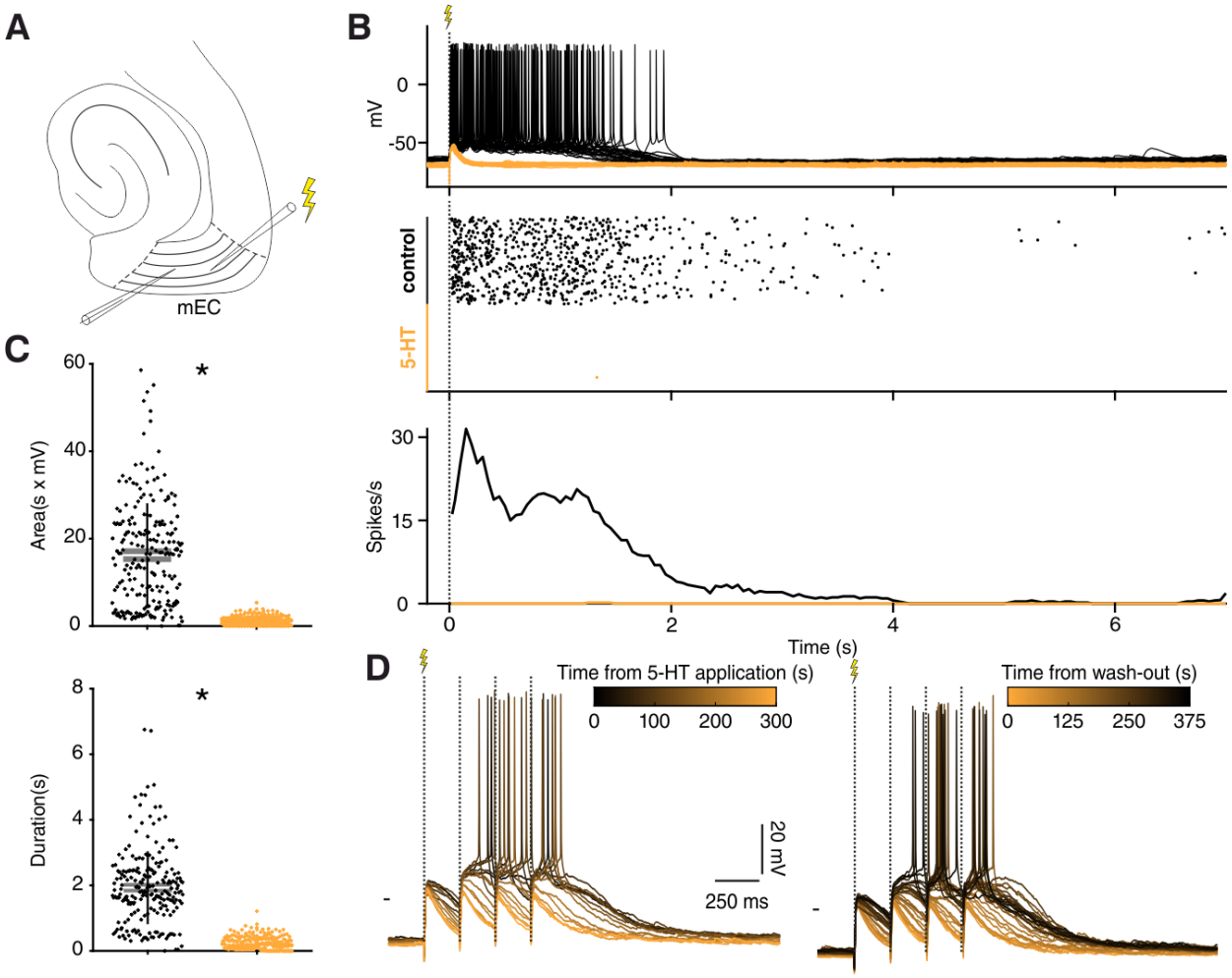

644 **Figure 3–figure supplement 2. 5-HT suppresses evoked up-states.**
645 **(A)** Experimental protocol: recording and stimulation electrode were placed in mEC layer 3,
646 stimulation electrode was located towards the lateral side of the slice. **(B)** Effect of electrical
647 stimulation before (black) and after 5-HT application (orange). 5-HT consistently suppresses
648 spiking, increasing the stimulation power up to 10 times (n = 40/80 in 4 neurons) had no rescue
649 effect. Top: voltage responses to electrical stimulation of a representative neuron. Middle:
650 summary spike raster plot before and after 5-HT application. Bottom: spike rate line histogram
651 **(C)** Scatter plot showing area (top, n = 8 neurons, mean $_{control}$ = 16.22 ± 0.80, , mean$_{5\text{-HT}}$ = 1.24
652 ± 0.97, $p < 10^{-4}$, Wilcoxon matched-pairs signed rank test) and duration (bottom, n = 8
653 neurons, mean $_{control}$ = 1.92 ± 0.07, , mean$_{5\text{-HT}}$ = 0.24 ± 0.01, , $p < 10^{-4}$, Wilcoxon matched-
654 pairs signed rank test) of evoked up-states before (black) and after 5-HT application (orange).
655 **(D)** Representative voltage responses to 1 second 4 Hz stimulation following wash-in (left) and
656 wash-out (right) of 5-HT. 5-HT prevents spiking from input summation.

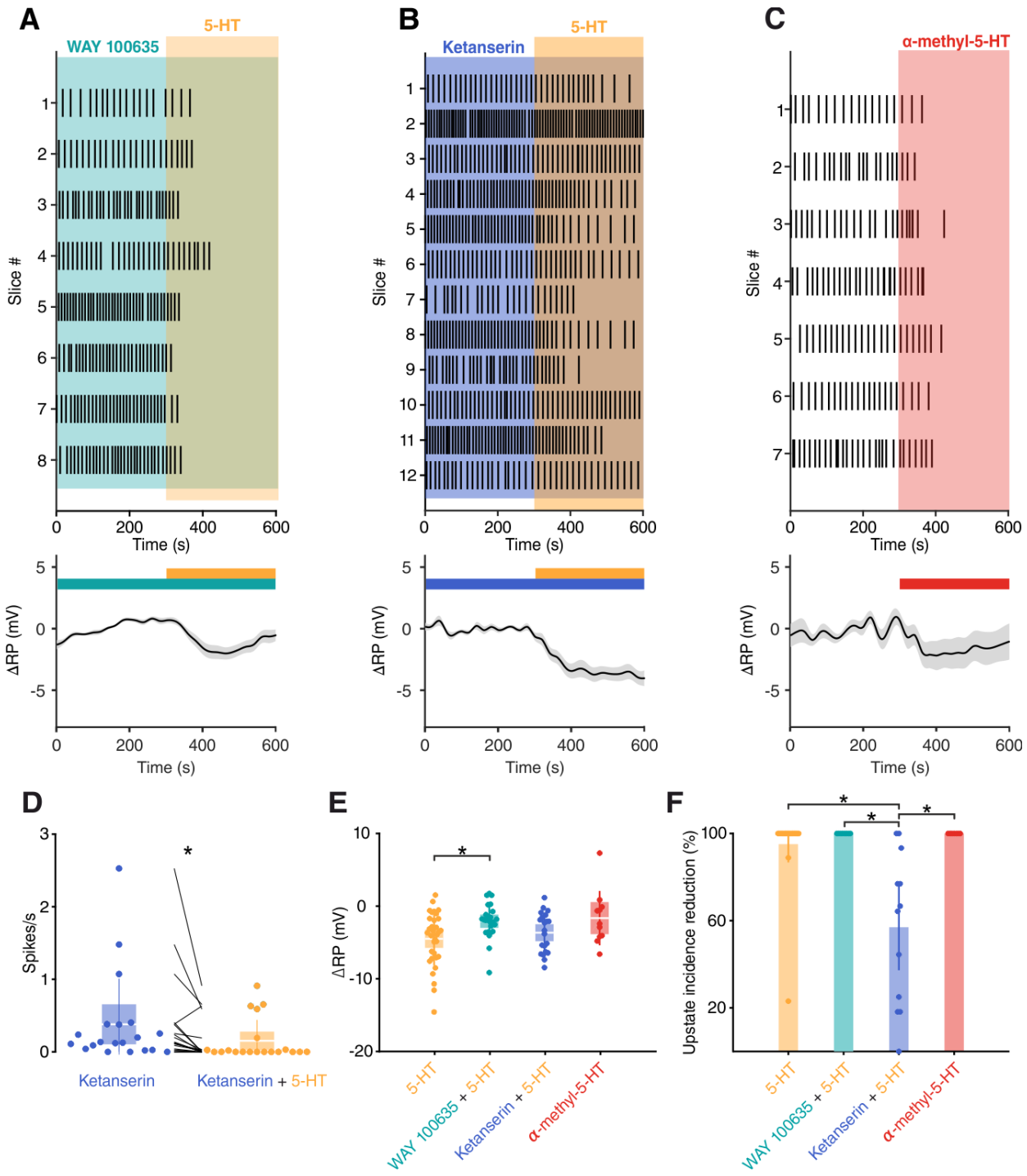

Figure 3–figure supplement 3. 5-HT$_{2A}$Rs are involved in 5-HT mediated SO suppression. **(A)** Top: Up-state raster plot during application of WAY 100635 (5-HT$_{1A}$ antagonist) + 5-HT. Bottom: Change in RP in putative excitatory cells after application of WAY 100635 (5-HT$_{1A}$ antagonist) + 5-HT (n = 25 cells). **(B)** Top: Up-state raster plot during application of ketanserin (5-HT$_{2A}$ antagonist) + 5-HT. Bottom: Change in RP in putative excitatory cells after application of ketanserin (5-HT$_{2A}$ antagonist) + 5-HT (n = 21 cells). **(C)** Top: Up-state raster plot during application of α-methyl-5-HT (5-HT$_2$ agonist). Bottom: Change in RP in putative excitatory cells after application of α-methyl-5-HT (5-HT$_2$ agonist) (n = 11 cells). **(D)** Dot plot showing spiking rate before and after ketanserin + 5-HT (n=20, ketanserin: 0.38 ± 0.14 spikes/s, ketanserin + 5-HT: 0.15 ± 0.06 spikes/s, p= 0.011, Wilcoxon signed rank test). **(E)** Dot plot showing change in RP for each pharmacological condition (5-HT: -4.52 ± 0.64 mV, WAY + 5-

668 HT: -2.09 ± 0.47 mV, ketanserin + 5-HT: -3.68 ± 0.60 mV and α-methyl-5-HT: -1.67 ± 1.13
669 mV; $p = 0.0329$, Kruskal-Wallis with Dunn's multiple comparisons test). **(F)** Dot plot showing
670 percentage reduction of up-states incidence for each pharmacological condition (5-HT: 95 ±
671 4 %, WAY + 5-HT: 100 ± 0 %, ketanserin + 5-HT: 57 ± 10.1 % and α-methyl-5-HT: 100 ± 0
672 %; $p < 10^{-4}$, Kruskal-Wallis with Dunn's multiple comparisons test).
673

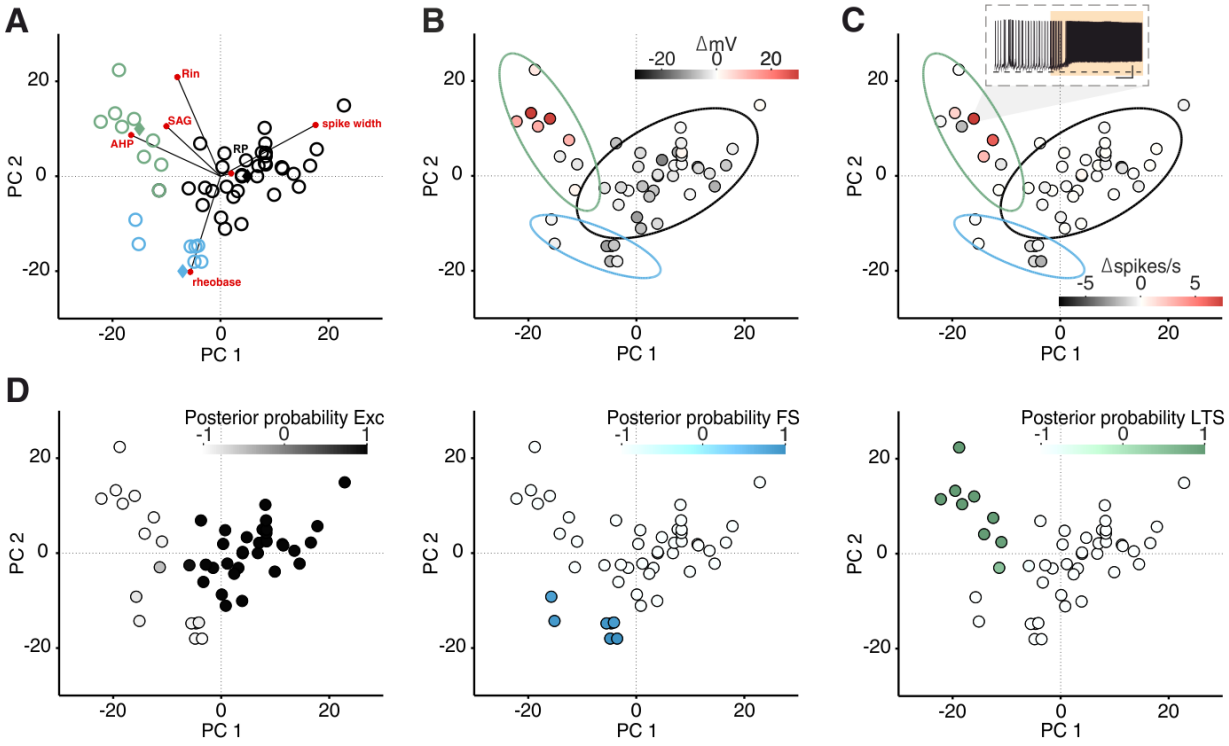

Figure 3–figure supplement 4. LTS neurons are depolarized by 5-HT.
(A) PCA projection plot of all the cells recorded. Cells are color coded according to group identity: excitatory (black), fast spiking (blue), low-threshold spiking (orange) and layer II stellate (grey). Empty circles represent PCA loadings. **(B)** PCA projection plot color coded according to ΔRP after 5-HT application. Inset shows a recording from one LTS neuron during 5-HT application. Scale bars: 20 mV, 25 s. Dotted line showing -70 mV. **(C)** PCA projection plot color coded according to Δspikes/s after 5-HT application. **(D)** Posterior probability of being classified as Exc, FS or LTS.

A

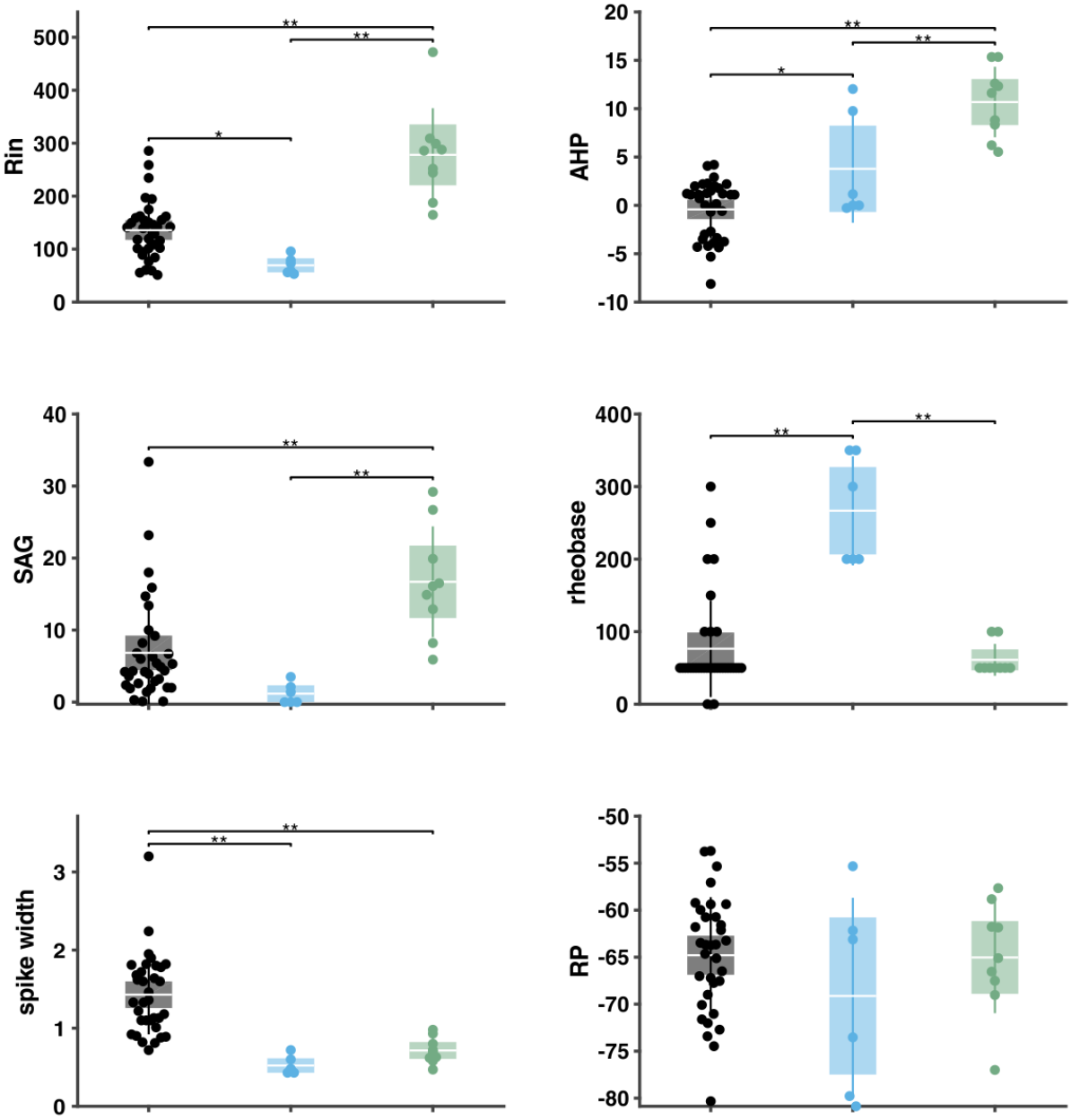

B

	Exc	FS	LTS
Rin	277.97 ± 57.52	69.38 ± 13.20	135.77 ± 18.47
AHP	10.68 ± 2.38	3.78 ± 4.46	-0.42 ± 1.00
SAG	16.70 ± 5.03	1.17 ± 1.16	6.84 ± 2.40
RP	61.11 ± 14.40	266.67 ± 60.23	76.47 ± 22.37
Rheobase	0.71 ± 0.11	0.52 ± 0.09	1.43 ± 0.17
Spike width	-65.03 ± 3.87	-69.13 ± 8.36	-64.80 ± 2.08

Figure 3–figure supplement 5. Excitatory, fast-spiking and LTS cells have unique sets of electrophysiological features.

(A) Box plot showing the values of input resistance (R_{in}), delta after-hyperpolarization (ΔAHP), SAG, RP, rheobase and spike width of excitatory (Exc, black), fast spiking (FS, blue) and low-

687 threshold spiking (LTS, green) cells ($n_{EXC} = 33$, $n_{FS} = 6$, $n_{LTS} = 9$; asterisk means $p < 0.05$, double
688 asterisk means $p < 0.01$). **(B)** Table showing values plotted in (A).
689

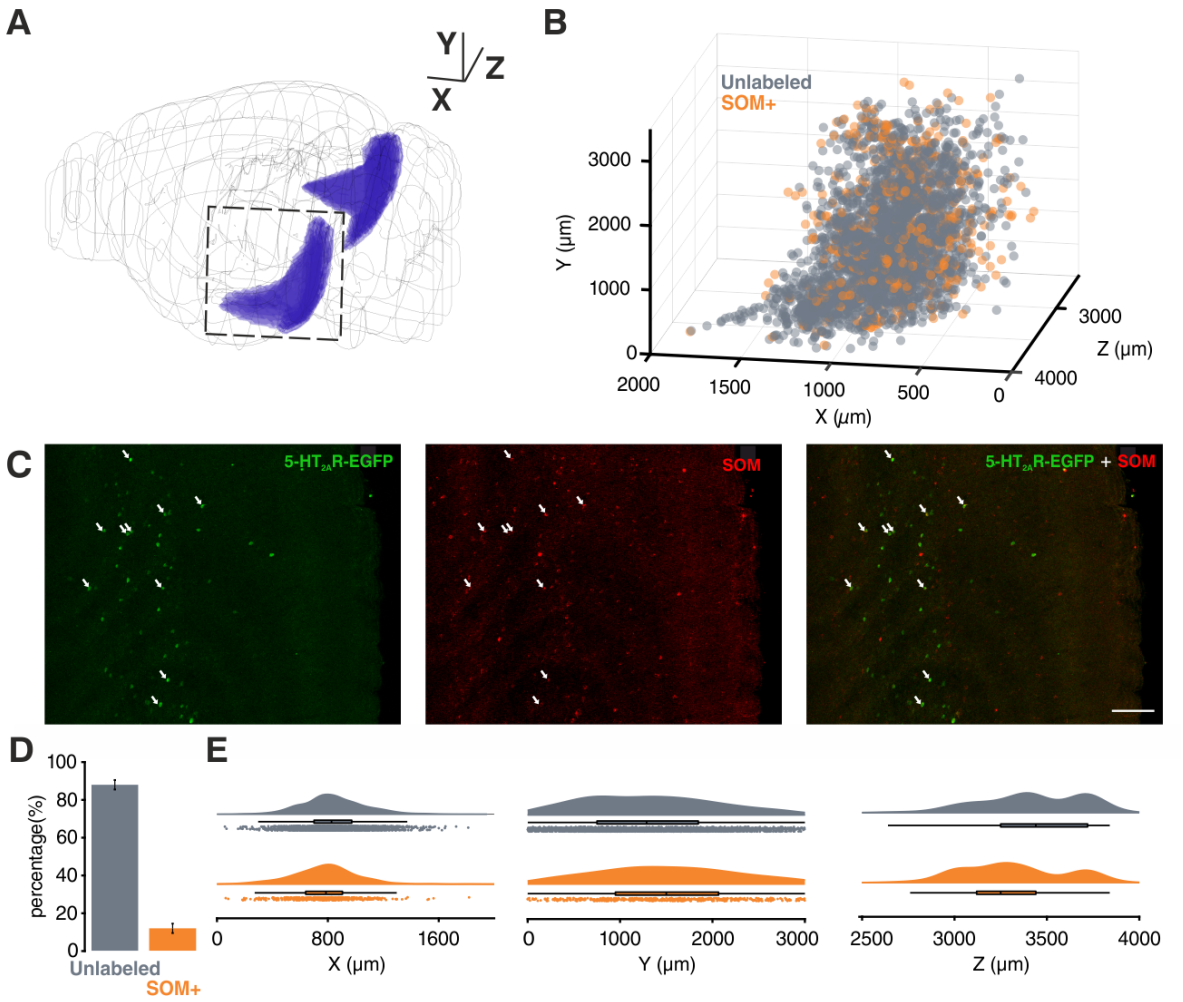

690 **Figure 3–figure supplement 6. Spatial localization of 5-HT$_{2A}$R positive cells in EC.**
691 **(A)** 3D visualization of EC (purple). **(B)** 3D localization of all the 5-HT$_{2A}$R positive cells detected
692 in EC using same perspective as (A). **(C** and **D)** Co-localization of 5-HT$_{2A}$R and Som, arrows
693 point to colocalized cells (scale bar: 100 µm, n $_{animals}$= 7, total number of 5-HT$_{2A}$R positive cells
694 = 3570, average number of 5-HT$_{2A}$R positive cells per animal = 510 ± 80.32). **(E)** Spatial
695 distribution of 5-HT$_{2A}$R positive cells and colocalized cells along the 3 dimensions depicted in
696 (A) (Z dimension centered on the midline).
697

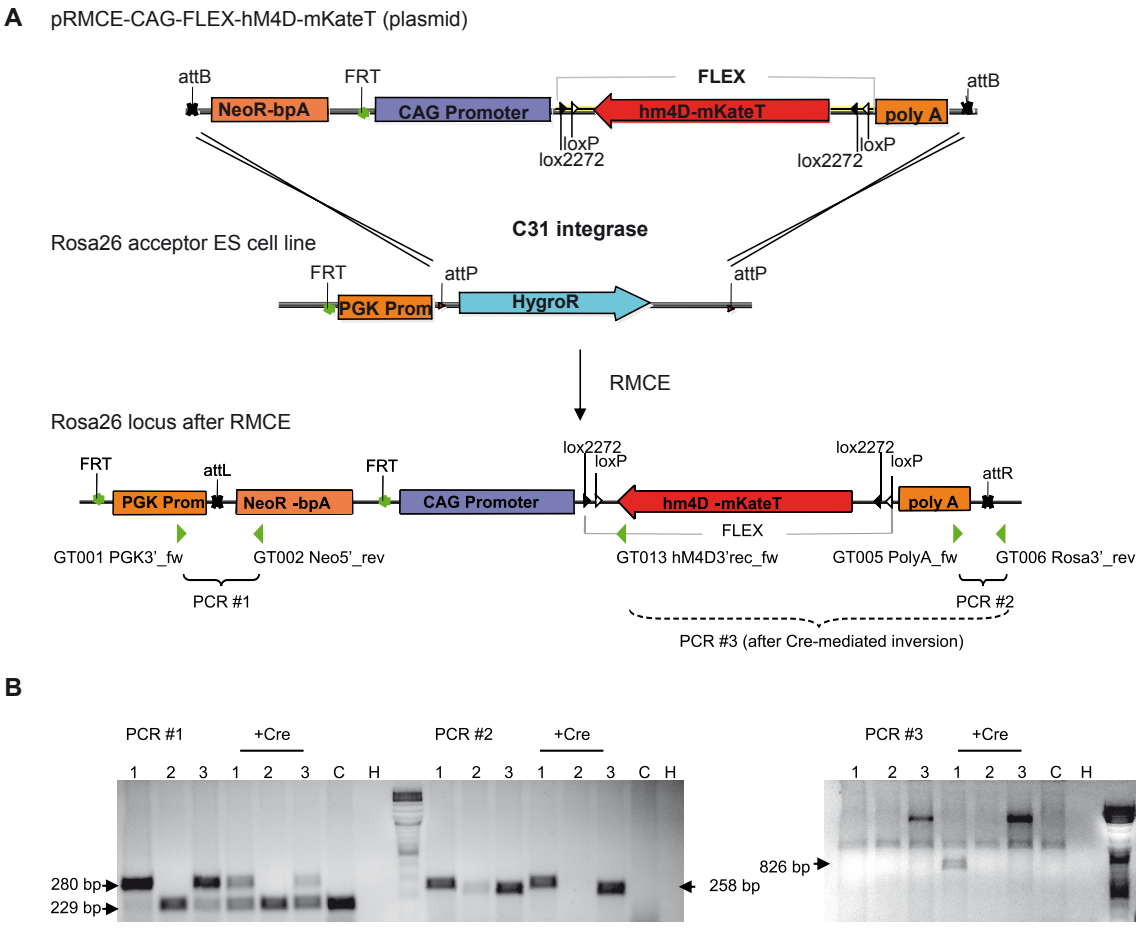

Figure 4–figure supplement 1. Vector construction and RMCE for the generation of a transgenic mouse line with Cre-conditional hM4Di expression.

(A) The coding sequence of hM4Di-mKate flanked by two opposing *loxP* and *lox2272* sites was placed in reverse orientation to the CAG- promoter in the pRMCE. In the acceptor ES cells the ROSA26 allele harbours a PGK promoter driving the hygromycin selection marker, flanked by two attP sites. RMCE by C31int replaces the hygromycin resistance by the neomycin resistance of the donor vector. Location of primer binding sites in the Rosa26-hM4Di locus is indicated by green triangles. **(B)** Identification of successful genomic integration events and Cre-mediated inversion of the hM4Di coding sequence by PCRs. PCR 1 and PCR 2 test for correct integration of the 5' and 3' end of the construct into the ROSA26 locus. The lower band in PCR 1 results from the Neomycin resistance cassette of the feeder cells in the ES cell culture. PCR 3 tests for successful recombination of the FLEX site by Cre. A successful Cre-mediated recombination of the FLEX cassette was observed for clone 1, resulting in an 826 bp product in PCR 3. C: control cells (not electroporated), H: H_2O input.

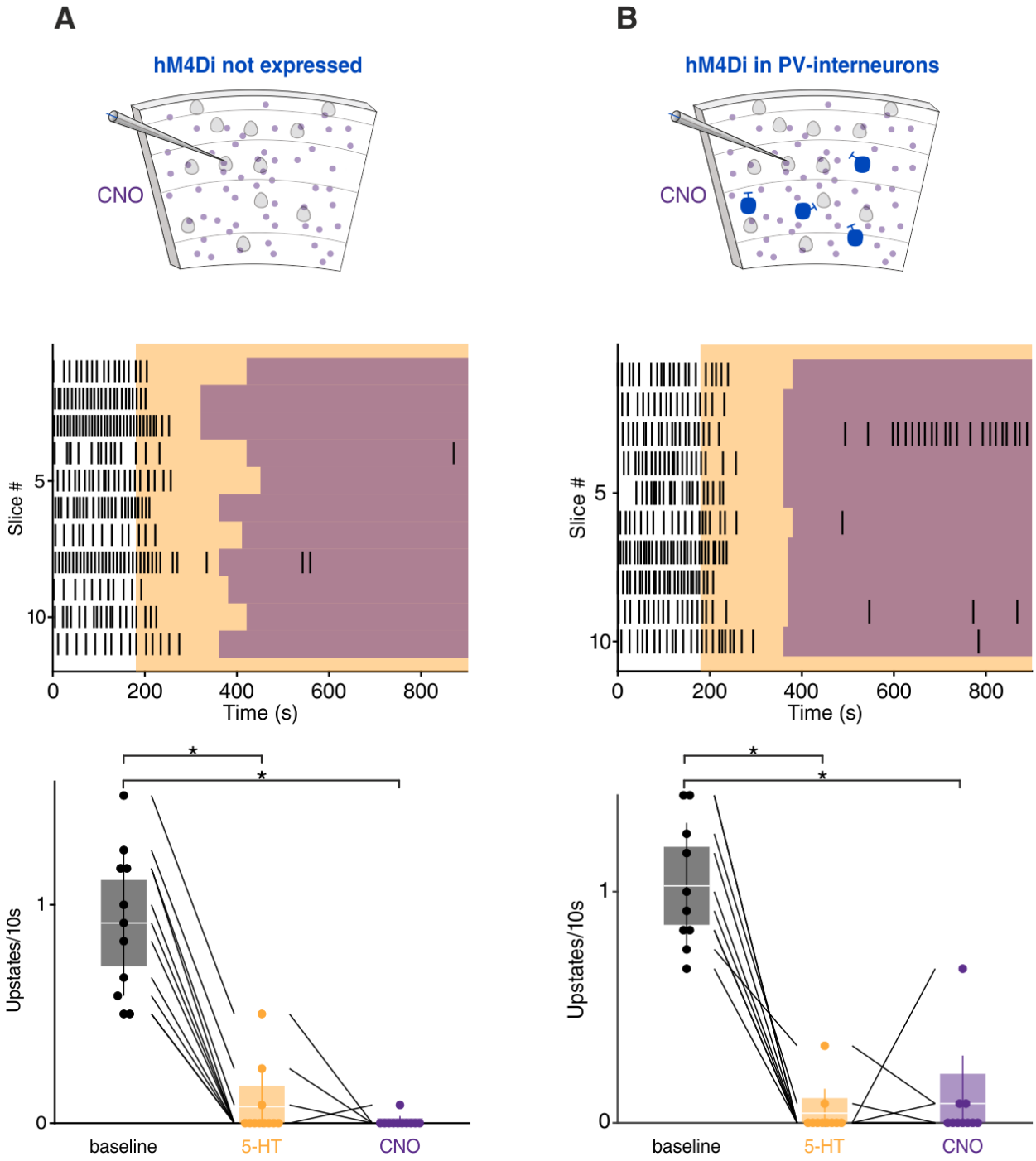

Figure 5–figure supplement 1. CNO application in wildtype littermates and PV-hM4Di mice.

(A) CNO application in wildtype littermates. Top: Experimental protocol. Orange box represents 5-HT and purple boxes represent CNO application. Bottom: Up-state incidence during 5-HT and 5-HT+CNO application, patches represent 95% confidence interval, lines represent standard deviation (n = 11 cells in 4 mice, mean $_{baseline}$ = 0.91 ± 0.10, mean $_{5\text{-}HT}$ = 0.09 ± 0.04, mean $_{CNO}$ = 0.01 ± 0.01, p $_{baseline\ vs\ 5\text{-}HT}$ = 0.0004, p $_{baseline\ vs\ CNO}$ < 10^{-4}, Kruskal-Wallis test) **(B)** Same as (A) but in in PV-hM4Di mice (n = 10 cells in 4 mice, mean $_{baseline}$ = 1.02 ± 0.08, mean$_{5\text{-}HT}$ = 0.04 ± 0.03, mean $_{CNO}$ = 0.08 ± 0.07, p $_{baseline\ vs\ 5\text{-}HT}$ < 10^{-4}, p $_{baseline\ vs\ CNO}$ = 0.0003, Kruskal-Wallis test).

References

ABI-SAAB, W. M., BUBSER, M., ROTH, R. H. & DEUTCH, A. Y. 1999. 5-HT2 receptor regulation of extracellular GABA levels in the prefrontal cortex. *Neuropsychopharmacology,* 20**,** 92-6.

ANTOINE, M. W., LANGBERG, T., SCHNEPEL, P. & FELDMAN, D. E. 2019. Increased Excitation-Inhibition Ratio Stabilizes Synapse and Circuit Excitability in Four Autism Mouse Models. *Neuron,* 101**,** 648-661.e4.

ARMBRUSTER, B. N., LI, X., PAUSCH, M. H., HERLITZE, S. & ROTH, B. L. 2007. Evolving the lock to fit the key to create a family of G protein-coupled receptors potently activated by an inert ligand. *Proc Natl Acad Sci U S A,* 104**,** 5163-8.

ASHBY, C. R., JR., JIANG, L. H., KASSER, R. J. & WANG, R. Y. 1990. Electrophysiological characterization of 5-hydroxytryptamine2 receptors in the rat medial prefrontal cortex. *J Pharmacol Exp Ther,* 252**,** 171-8.

ATHILINGAM, J. C., BEN-SHALOM, R., KEESHEN, C. M., SOHAL, V. S. & BENDER, K. J. 2017. Serotonin enhances excitability and gamma frequency temporal integration in mouse prefrontal fast-spiking interneurons. *eLife,* 6**,** e31991.

AZIMI, Z., BARZAN, R., SPOIDA, K., SURDIN, T., WOLLENWEBER, P., MARK, M. D., HERLITZE, S. & JANCKE, D. 2020. Separable gain control of ongoing and evoked activity in the visual cortex by serotonergic input. *eLife,* 9**,** e53552.

BARTHÓ, P., HIRASE, H., MONCONDUIT, L., ZUGARO, M., HARRIS, K. D. & BUZSÁKI, G. 2004. Characterization of neocortical principal cells and interneurons by network interactions and extracellular features. *J Neurophysiol,* 92**,** 600-8.

CARHART-HARRIS, R. L. & FRISTON, K. J. 2019. REBUS and the Anarchic Brain: Toward a Unified Model of the Brain Action of Psychedelics. *Pharmacol Rev,* 71**,** 316-344.

CARHART-HARRIS, R. L., MUTHUKUMARASWAMY, S., ROSEMAN, L., KAELEN, M., DROOG, W., MURPHY, K., TAGLIAZUCCHI, E., SCHENBERG, E. E., NEST, T., ORBAN, C., LEECH, R., WILLIAMS, L. T., WILLIAMS, T. M., BOLSTRIDGE, M., SESSA, B., MCGONIGLE, J., SERENO, M. I., NICHOLS, D., HELLYER, P. J., HOBDEN, P., EVANS, J., SINGH, K. D., WISE, R. G., CURRAN, H. V., FEILDING, A. & NUTT, D. J. 2016. Neural correlates of the LSD experience revealed by multimodal neuroimaging. *Proc Natl Acad Sci U S A,* 113**,** 4853-8.

CHALMERS, D. T. & WATSON, S. J. 1991. Comparative anatomical distribution of 5-HT1A receptor mRNA and 5-HT1A binding in rat brain--a combined in situ hybridisation/in vitro receptor autoradiographic study. *Brain Res,* 561**,** 51-60.

CHEN, N., SUGIHARA, H. & SUR, M. 2015. An acetylcholine-activated microcircuit drives temporal dynamics of cortical activity. *Nat Neurosci,* 18**,** 892-902.

DE BLASI, S., CIBA, M., BAHMER, A. & THIELEMANN, C. 2019. Total spiking probability edges: A cross-correlation based method for effective connectivity estimation of cortical spiking neurons. *J Neurosci Methods,* 312**,** 169-181.

762 DESCARRIES, L., RIAD, M. & PARENT, M. 2010. CHAPTER 1.4 - Ultrastructure of the
763 Serotonin Innervation in the Mammalian Central Nervous System. *In:* MÜLLER, C. P.
764 & JACOBS, B. L. (eds.) *Handbook of Behavioral Neuroscience.* Elsevier.

765 FANSELOW, E. E., RICHARDSON, K. A. & CONNORS, B. W. 2008. Selective, state-
766 dependent activation of somatostatin-expressing inhibitory interneurons in mouse
767 neocortex. *J Neurophysiol,* 100**,** 2640-52.

768 FREI, E., GAMMA, A., PASCUAL-MARQUI, R., LEHMANN, D., HELL, D. & VOLLENWEIDER,
769 F. X. 2001. Localization of MDMA-induced brain activity in healthy volunteers using
770 low resolution brain electromagnetic tomography (LORETA). *Hum Brain Mapp,* 14**,**
771 152-65.

772 FUNK, C. M., PEELMAN, K., BELLESI, M., MARSHALL, W., CIRELLI, C. & TONONI, G.
773 2017. Role of Somatostatin-Positive Cortical Interneurons in the Generation of Sleep
774 Slow Waves. *J Neurosci,* 37**,** 9132-9148.

775 GIBSON, J. R., BEIERLEIN, M. & CONNORS, B. W. 1999. Two networks of electrically
776 coupled inhibitory neurons in neocortex. *Nature,* 402**,** 75-9.

777 GRANDJEAN, J., CORCOBA, A., KAHN, M. C., UPTON, A. L., DENERIS, E. S., SEIFRITZ, E.,
778 HELMCHEN, F., MANN, E. O., RUDIN, M. & SAAB, B. J. 2019. A brain-wide
779 functional map of the serotonergic responses to acute stress and fluoxetine. *Nat*
780 *Commun,* 10**,** 350.

781 GREEN, A. R., MECHAN, A. O., ELLIOTT, J. M., O'SHEA, E. & COLADO, M. I. 2003. The
782 Pharmacology and Clinical Pharmacology of 3,4-Methylenedioxymethamphetamine
783 (MDMA, “Ecstasy”). *Pharmacological Reviews,* 55**,** 463-508.

784 HARDEBO, J. E. & OWMAN, C. 1980. Barrier mechanisms for neurotransmitter monoamines
785 and their precursors at the blood-brain interface. *Ann Neurol,* 8**,** 1-31.

786 HARDY, A., PALOUZIER-PAULIGNAN, B., DUCHAMP, A., ROYET, J. P. & DUCHAMP-
787 VIRET, P. 2005. 5-Hydroxytryptamine action in the rat olfactory bulb: in vitro
788 electrophysiological patch-clamp recordings of juxtaglomerular and mitral cells.
789 *Neuroscience,* 131**,** 717-31.

790 HARRIS, K. D. & THIELE, A. 2011. Cortical state and attention. *Nat Rev Neurosci,* 12**,** 509-
791 23.

792 HAYES, D. J. & GREENSHAW, A. J. 2011. 5-HT receptors and reward-related behaviour: a
793 review. *Neurosci Biobehav Rev,* 35**,** 1419-49.

794 HITZ, C., STEUBER-BUCHBERGER, P., DELIC, S., WURST, W. & KUHN, R. 2009.
795 Generation of shRNA transgenic mice. *Methods Mol Biol,* 530**,** 101-29.

796 HITZ, C., WURST, W. & KUHN, R. 2007. Conditional brain-specific knockdown of MAPK
797 using Cre/loxP regulated RNA interference. *Nucleic Acids Res,* 35**,** e90.

798 KAUR, S., JUNEK, A., BLACK, M. A. & SEMBA, K. 2008. Effects of ibotenate and 192IgG-
799 saporin lesions of the nucleus basalis magnocellularis/substantia innominata on
800 spontaneous sleep and wake states and on recovery sleep after sleep deprivation in
801 rats. *J Neurosci,* 28**,** 491-504.

KOMETER, M., POKORNY, T., SEIFRITZ, E. & VOLLEINWEIDER, F. X. 2015. Psilocybin-induced spiritual experiences and insightfulness are associated with synchronization of neuronal oscillations. *Psychopharmacology (Berl),* 232**,** 3663-76.

KUYPERS, K. P. C., DE LA TORRE, R., FARRE, M., PIZARRO, N., XICOTA, L. & RAMAEKERS, J. G. 2018. MDMA-induced indifference to negative sounds is mediated by the 5-HT2A receptor. *Psychopharmacology (Berl),* 235**,** 481-490.

KVITSIANI, D., RANADE, S., HANGYA, B., TANIGUCHI, H., HUANG, J. Z. & KEPECS, A. 2013. Distinct behavioural and network correlates of two interneuron types in prefrontal cortex. *Nature,* 498**,** 363-6.

LANSBERGEN, M. M., DUMONT, G. J. H., VAN GERVEN, J. M. A., BUITELAAR, J. K. & VERKES, R.-J. 2011. Acute effects of MDMA (3,4-methylenedioxymethamphetamine) on EEG oscillations: alone and in combination with ethanol or THC (delta-9-tetrahydrocannabinol). *Psychopharmacology,* 213**,** 745-756.

LEE, S. H. & DAN, Y. 2012. Neuromodulation of brain states. *Neuron,* 76**,** 209-22.

LIECHTI, M. E., SAUR, M. R., GAMMA, A., HELL, D. & VOLLENWEIDER, F. X. 2000. Psychological and Physiological Effects of MDMA ("Ecstasy") after Pretreatment with the 5-HT2 Antagonist Ketanserin in Healthy Humans. *Neuropsychopharmacology,* 23**,** 396-404.

LIN, L. C. & SIBILLE, E. 2015. Somatostatin, neuronal vulnerability and behavioral emotionality. *Mol Psychiatry,* 20**,** 377-87.

LOTTEM, E., LÖRINCZ, M. L. & MAINEN, Z. F. 2016. Optogenetic Activation of Dorsal Raphe Serotonin Neurons Rapidly Inhibits Spontaneous But Not Odor-Evoked Activity in Olfactory Cortex. *J Neurosci,* 36**,** 7-18.

MAREK, G. J. & AGHAJANIAN, G. K. 1994. Excitation of interneurons in piriform cortex by 5-hydroxytryptamine: blockade by MDL 100,907, a highly selective 5-HT2A receptor antagonist. *Eur J Pharmacol,* 259**,** 137-41.

MAREK, G. J., CARPENTER, L. L., MCDOUGLE, C. J. & PRICE, L. H. 2003. Synergistic action of 5-HT2A antagonists and selective serotonin reuptake inhibitors in neuropsychiatric disorders. *Neuropsychopharmacology,* 28**,** 402-12.

MARTIN, D. A. & NICHOLS, C. D. 2016. Psychedelics Recruit Multiple Cellular Types and Produce Complex Transcriptional Responses Within the Brain. *EBioMedicine,* 11**,** 262-277.

MCGINTY, D. J. & HARPER, R. M. 1976. Dorsal raphe neurons: depression of firing during sleep in cats. *Brain Research,* 101**,** 569-575.

MELTZER, H. Y. 1999. The role of serotonin in antipsychotic drug action. *Neuropsychopharmacology,* 21**,** 106s-115s.

MICHAIEL, A. M., PARKER, P. R. L. & NIELL, C. M. 2019. A Hallucinogenic Serotonin-2A Receptor Agonist Reduces Visual Response Gain and Alters Temporal Dynamics in Mouse V1. *Cell Rep,* 26**,** 3475-3483.e4.

MONTI, J. M. 2011. Serotonin control of sleep-wake behavior. *Sleep Med Rev,* 15**,** 269-81.

MURAYAMA, M., PÉREZ-GARCI, E., NEVIAN, T., BOCK, T., SENN, W. & LARKUM, M. E. 2009. Dendritic encoding of sensory stimuli controlled by deep cortical interneurons. *Nature,* 457**,** 1137-1141.

MUTHUKUMARASWAMY, S. D., CARHART-HARRIS, R. L., MORAN, R. J., BROOKES, M. J., WILLIAMS, T. M., ERRTIZOE, D., SESSA, B., PAPADOPOULOS, A., BOLSTRIDGE, M., SINGH, K. D., FEILDING, A., FRISTON, K. J. & NUTT, D. J. 2013. Broadband cortical desynchronization underlies the human psychedelic state. *J Neurosci,* 33**,** 15171-83.

MUZERELLE, A., SCOTTO-LOMASSESE, S., BERNARD, J. F., SOIZA-REILLY, M. & GASPAR, P. 2016. Conditional anterograde tracing reveals distinct targeting of individual serotonin cell groups (B5–B9) to the forebrain and brainstem. *Brain Structure and Function,* 221**,** 535-561.

NAKAI, N., NAGANO, M., SAITOW, F., WATANABE, Y., KAWAMURA, Y., KAWAMOTO, A., TAMADA, K., MIZUMA, H., ONOE, H., WATANABE, Y., MONAI, H., HIRASE, H., NAKATANI, J., INAGAKI, H., KAWADA, T., MIYAZAKI, T., WATANABE, M., SATO, Y., OKABE, S., KITAMURA, K., KANO, M., HASHIMOTO, K., SUZUKI, H. & TAKUMI, T. 2017. Serotonin rebalances cortical tuning and behavior linked to autism symptoms in 15q11-13 CNV mice. *Sci Adv,* 3**,** e1603001.

NESKE, G. T. 2015. The Slow Oscillation in Cortical and Thalamic Networks: Mechanisms and Functions. *Front Neural Circuits,* 9**,** 88.

NESKE, G. T., PATRICK, S. L. & CONNORS, B. W. 2015. Contributions of diverse excitatory and inhibitory neurons to recurrent network activity in cerebral cortex. *J Neurosci,* 35**,** 1089-105.

NICHOLS, D. E. 2016. Psychedelics. *Pharmacol Rev,* 68**,** 264-355.

NICHOLS, D. E. & NICHOLS, C. D. 2008. Serotonin Receptors. *Chemical Reviews,* 108**,** 1614-1641.

NIETHARD, N., NGO, H. V., EHRLICH, I. & BORN, J. 2018. Cortical circuit activity underlying sleep slow oscillations and spindles. *Proc Natl Acad Sci U S A,* 115**,** E9220-e9229.

OBERMAYER, J., HEISTEK, T. S., KERKHOFS, A., GORIOUNOVA, N. A., KROON, T., BAAYEN, J. C., IDEMA, S., TESTA-SILVA, G., COUEY, J. J. & MANSVELDER, H. D. 2018. Lateral inhibition by Martinotti interneurons is facilitated by cholinergic inputs in human and mouse neocortex. *Nat Commun,* 9**,** 4101.

OIKONOMOU, G., ALTERMATT, M., ZHANG, R. W., COUGHLIN, G. M., MONTZ, C., GRADINARU, V. & PROBER, D. A. 2019. The Serotonergic Raphe Promote Sleep in Zebrafish and Mice. *Neuron,* 103**,** 686-701.e8.

PANTAZOPOULOS, H., WISEMAN, J. T., MARKOTA, M., EHRENFELD, L. & BERRETTA, S. 2017. Decreased Numbers of Somatostatin-Expressing Neurons in the Amygdala of Subjects With Bipolar Disorder or Schizophrenia: Relationship to Circadian Rhythms. *Biol Psychiatry,* 81**,** 536-547.

PETZOLD, G. C., HAGIWARA, A. & MURTHY, V. N. 2009. Serotonergic modulation of odor input to the mammalian olfactory bulb. *Nature Neuroscience,* 12**,** 784-791.

PRELLER, K. H., BURT, J. B., JI, J. L., SCHLEIFER, C. H., ADKINSON, B. D., STAMPFLI, P., SEIFRITZ, E., REPOVS, G., KRYSTAL, J. H., MURRAY, J. D., VOLLENWEIDER, F. X. & ANTICEVIC, A. 2018. Changes in global and thalamic brain connectivity in LSD-induced altered states of consciousness are attributable to the 5-HT2A receptor. *Elife,* 7.

PUIG, M. V., WATAKABE, A., USHIMARU, M., YAMAMORI, T. & KAWAGUCHI, Y. 2010. Serotonin modulates fast-spiking interneuron and synchronous activity in the rat prefrontal cortex through 5-HT1A and 5-HT2A receptors. *J Neurosci,* 30**,** 2211-22.

RANGANATHAN, G. N., APOSTOLIDES, P. F., HARNETT, M. T., XU, N. L., DRUCKMANN, S. & MAGEE, J. C. 2018. Active dendritic integration and mixed neocortical network representations during an adaptive sensing behavior. *Nat Neurosci,* 21**,** 1583-1590.

RENART, A., DE LA ROCHA, J., BARTHO, P., HOLLENDER, L., PARGA, N., REYES, A. & HARRIS, K. D. 2010. The asynchronous state in cortical circuits. *Science,* 327**,** 587-90.

ROTHMAN, R. B. & BAUMANN, M. H. 2002. Therapeutic and adverse actions of serotonin transporter substrates. *Pharmacol Ther,* 95**,** 73-88.

ROUX, L., STARK, E., SJULSON, L. & BUZSAKI, G. 2014. In vivo optogenetic identification and manipulation of GABAergic interneuron subtypes. *Curr Opin Neurobiol,* 26**,** 88-95.

SANCHEZ-VIVES, M. V., MASSIMINI, M. & MATTIA, M. 2017. Shaping the Default Activity Pattern of the Cortical Network. *Neuron,* 94**,** 993-1001.

SCHMITZ, D., GLOVELI, T., EMPSON, R. M., DRAGUHN, A. & HEINEMANN, U. 1998. Serotonin reduces synaptic excitation in the superficial medial entorhinal cortex of the rat via a presynaptic mechanism. *J Physiol,* 508 (Pt 1)**,** 119-29.

SCHNUTGEN, F., DOERFLINGER, N., CALLEJA, C., WENDLING, O., CHAMBON, P. & GHYSELINCK, N. B. 2003. A directional strategy for monitoring Cre-mediated recombination at the cellular level in the mouse. *Nat Biotechnol,* 21**,** 562-5.

SEILLIER, L., LORENZ, C., KAWAGUCHI, K., OTT, T., NIEDER, A., POURRIAHI, P. & NIENBORG, H. 2017. Serotonin Decreases the Gain of Visual Responses in Awake Macaque V1. *J Neurosci,* 37**,** 11390-11405.

SENZAI, Y., FERNANDEZ-RUIZ, A. & BUZSAKI, G. 2019. Layer-Specific Physiological Features and Interlaminar Interactions in the Primary Visual Cortex of the Mouse. *Neuron,* 101**,** 500-513 e5.

SHAMASH, P., CARANDINI, M., HARRIS, K. & STEINMETZ, N. 2018. A tool for analyzing electrode tracks from slice histology. *bioRxiv***,** 447995.

SHELDON, P. W. & AGHAJANIAN, G. K. 1990. Serotonin (5-HT) induces IPSPs in pyramidal layer cells of rat piriform cortex: evidence for the involvement of a 5-HT2-activated interneuron. *Brain Res,* 506**,** 62-9.

SIPPY, T. & YUSTE, R. 2013. Decorrelating action of inhibition in neocortical networks. *J Neurosci,* 33**,** 9813-30.

SMITH, S. L., SMITH, I. T., BRANCO, T. & HÄUSSER, M. 2013. Dendritic spikes enhance stimulus selectivity in cortical neurons in vivo. *Nature,* 503**,** 115-120.

STERIADE, M., NUNEZ, A. & AMZICA, F. 1993. A novel slow (< 1 Hz) oscillation of neocortical neurons in vivo: depolarizing and hyperpolarizing components. *J Neurosci,* 13**,** 3252-65.

STRINGER, C., PACHITARIU, M., STEINMETZ, N. A., OKUN, M., BARTHO, P., HARRIS, K. D., SAHANI, M. & LESICA, N. A. 2016. Inhibitory control of correlated intrinsic variability in cortical networks. *Elife,* 5.

STURGILL, J. F. & ISAACSON, J. S. 2015. Somatostatin cells regulate sensory response fidelity via subtractive inhibition in olfactory cortex. *Nat Neurosci,* 18**,** 531-5.

TAHVILDARI, B., WOLFEL, M., DUQUE, A. & MCCORMICK, D. A. 2012. Selective functional interactions between excitatory and inhibitory cortical neurons and differential contribution to persistent activity of the slow oscillation. *J Neurosci,* 32**,** 12165-79.

TAKAHASHI, N., OERTNER, T. G., HEGEMANN, P. & LARKUM, M. E. 2016. Active cortical dendrites modulate perception. *Science,* 354**,** 1587-1590.

TANG, Z.-Q. & TRUSSELL, L. O. 2017. Serotonergic Modulation of Sensory Representation in a Central Multisensory Circuit Is Pathway Specific. *Cell reports,* 20**,** 1844-1854.

TANIGUCHI, H., HE, M., WU, P., KIM, S., PAIK, R., SUGINO, K., KVITSIANI, D., FU, Y., LU, J., LIN, Y., MIYOSHI, G., SHIMA, Y., FISHELL, G., NELSON, S. B. & HUANG, Z. J. 2011. A resource of Cre driver lines for genetic targeting of GABAergic neurons in cerebral cortex. *Neuron,* 71**,** 995-1013.

TEIXEIRA, C. M., ROSEN, Z. B., SURI, D., SUN, Q., HERSH, M., SARGIN, D., DINCHEVA, I., MORGAN, A. A., SPIVACK, S., KROK, A. C., HIRSCHFELD-STOLER, T., LAMBE, E. K., SIEGELBAUM, S. A. & ANSORGE, M. S. 2018. Hippocampal 5-HT Input Regulates Memory Formation and Schaffer Collateral Excitation. *Neuron,* 98**,** 992-1004.e4.

TRAINITO, C., VON NICOLAI, C., MILLER, E. K. & SIEGEL, M. 2019. Extracellular Spike Waveform Dissociates Four Functionally Distinct Cell Classes in Primate Cortex. *Curr Biol*.

TREMBLAY, R., LEE, S. & RUDY, B. 2016. GABAergic Interneurons in the Neocortex: From Cellular Properties to Circuits. *Neuron,* 91**,** 260-92.

TURRIGIANO, G. 2011. Too many cooks? Intrinsic and synaptic homeostatic mechanisms in cortical circuit refinement. *Annu Rev Neurosci,* 34**,** 89-103.

UNDERWOOD, M. D., KASSIR, S. A., BAKALIAN, M. J., GALFALVY, H., DWORK, A. J., MANN, J. J. & ARANGO, V. 2018. Serotonin receptors and suicide, major depression, alcohol use disorder and reported early life adversity. *Translational Psychiatry,* 8**,** 279.

959 UPHOUSE, L. & GUPTARAK, J. 2010. Serotonin and sexual behavior. *Handbook of the*
960 *behavioral neurobiology of serotonin.* San Diego, CA, US: Elsevier Academic Press.

961 URBAN-CIECKO, J., FANSELOW, E. E. & BARTH, A. L. 2015. Neocortical somatostatin
962 neurons reversibly silence excitatory transmission via GABAb receptors. *Curr Biol,* 25**,**
963 722-31.

964 VAN STRIEN, N. M., CAPPAERT, N. L. & WITTER, M. P. 2009. The anatomy of memory: an
965 interactive overview of the parahippocampal-hippocampal network. *Nat Rev*
966 *Neurosci,* 10**,** 272-82.

967 VANDERWOLF, C. H. & BAKER, G. B. 1986. Evidence that serotonin mediates non-
968 cholinergic neocortical low voltage fast activity, non-cholinergic hippocampal
969 rhythmical slow activity and contributes to intelligent behavior. *Brain Res,* 374**,** 342-
970 56.

971 WILSON, N. R., RUNYAN, C. A., WANG, F. L. & SUR, M. 2012. Division and subtraction by
972 distinct cortical inhibitory networks in vivo. *Nature,* 488**,** 343-348.

973 WOOD, J., KIM, Y. & MOGHADDAM, B. 2012. Disruption of prefrontal cortex large scale
974 neuronal activity by different classes of psychotomimetic drugs. *J Neurosci,* 32**,**
975 3022-31.

976 WYSKIEL, D. R. & ANDRADE, R. 2016. Serotonin excites hippocampal CA1 GABAergic
977 interneurons at the stratum radiatum-stratum lacunosum moleculare border.
978 *Hippocampus,* 26**,** 1107-14.

979 ZHOU, F.-M. & HABLITZ, J. J. 1999. Activation of Serotonin Receptors Modulates Synaptic
980 Transmission in Rat Cerebral Cortex. *Journal of Neurophysiology,* 82**,** 2989-2999.

981